Atf3 links loss of epithelial polarity to defects in cell differentiation and cytoarchitecture

Colin D. Donohoe[1], Andreia Correia[1], Gábor Csordás[1], Marek Jindra[2], Corinna Klein[3,#a], Bianca Habermann[4,#b], Mirka Uhlirova[1,5*]

[1] Institute for Genetics and Cologne Excellence Cluster on Cellular Stress Responses in Aging-Associated Diseases (CECAD), University of Cologne, Cologne, 50931, Germany

[2] Biology Center, Czech Academy of Sciences, Ceske Budejovice, 37005, Czech Republic

[3] Max Planck Institute for Biology of Ageing, Cologne, 50931, Germany

[4] Max Planck Institute of Biochemistry, Martinsried, 82152, Germany

[5] Center for Molecular Medicine Cologne, University of Cologne, Cologne, 50931, Germany

* Corresponding author

E-mail: mirka.uhlirova@uni-koeln.de (MU)

[#a] current address: CECAD Lipidomics & Proteomics Facilities, Cologne, 50931, Germany

[#b] current address: Institut de Biologie du Développement de Marseille, 13288 Marseille, France

Short Title: Interaction between epithelial tumor suppressors and Atf3

Abstract

Interplay between apicobasal cell polarity modules and the cytoskeleton is critical for differentiation and integrity of epithelia. However, this coordination is poorly understood at the level of gene regulation by transcription factors. Here, we establish the *Drosophila activating transcription factor 3* (*atf3*) as a cell polarity response gene acting downstream of the membrane-associated Scribble polarity complex. Loss of the tumor suppressors Scribble or Dlg1 induces *atf3* expression via aPKC but independent of Jun-N-terminal kinase (JNK) signaling. Strikingly, removal of Atf3 from Dlg1 deficient cells restores polarized cytoarchitecture, levels and distribution of endosomal trafficking machinery, and differentiation. Conversely, excess Atf3 alters microtubule network, vesicular trafficking and the partition of polarity proteins along the apicobasal axis. Genomic and genetic approaches implicate Atf3 as a regulator of cytoskeleton organization and function, and identify *Lamin C* as one of its *bona fide* target genes. By affecting structural features and cell morphology, Atf3 functions in a manner distinct from other transcription factors operating downstream of disrupted cell polarity.

Author summary

Epithelial cells form sheets and line both the outside and inside of our body. Their proper development and function require the asymmetric distribution of cellular components from the top to the bottom, known as apicobasal polarization. As loss of polarity hallmarks a majority of cancers in humans understanding how epithelia respond to a collapse of the apicobasal axis is of great interest. Here, we show that in the fruit fly *Drosophila melanogaster*, the breakdown of epithelial polarity engages Activating transcription factor 3 (Atf3), a protein that directly binds the DNA and regulates gene expression. We demonstrate that many of the pathological consequences of disturbed polarity

require Atf3, as its loss in this context results in normalization of cellular architecture, vesicle trafficking and differentiation. Using unbiased genome-wide approaches we identify the genetic program controlled by Atf3 and experimentally verify select candidates. Given the evolutionary conservation of Atf3 between flies and man, we believe that our findings in the *Drosophila* model will contribute to a better understanding of diseases stemming from compromised epithelial polarity.

Introduction

Epithelia are sheets of highly polarized cells that represent the defining tissue type of metazoans. With their capacity to achieve various shapes and serve as selective barriers, epithelial tissues play vital roles in morphogenesis, tissue differentiation and compartmentalization, and intercellular signaling. The integrity and function of epithelia rely on the interplay between key polarity determinants and a highly ordered yet dynamic cytoskeleton, which ensures tissue plasticity and the asymmetric distribution of cellular components along the apicobasal polarity axis [1].

Genetic studies have established a network of evolutionarily conserved signaling pathways and effector molecules that govern the organization of epithelial cellular architecture. In particular, the basic leucine zipper (bZIP) transcription factors, including Jun, Fos, and Atf3, are important regulators of epithelial function from the fruit fly *Drosophila* to mammals [2-6]. During *Drosophila* development, expression of *atf3* is dynamic and under tight temporal constraints. Ectopic Atf3 activity in larval epidermal cells (LECs) disturbs epithelial morphogenesis of the adult abdomen, stemming from perturbed cytoskeleton dynamics and increased cell adhesion which prevent normal LEC extrusion [6].

The importance of finely tuned Atf3 expression during *Drosophila* development corresponds with the

role of mammalian ATF3 as a stress-response gene regulated at the level of mRNA expression by various stimuli, including genotoxic radiation, wounding, cytokines, nutrient deprivation, Toll signaling, oncogenes and inhibition of calcineurin-NFAT signaling [7-9]. Independent transcriptome analyses of *Drosophila* epithelia have shown deregulated *atf3* expression in wing imaginal discs lacking the conserved neoplastic tumor suppressor genes *scribble* (*scrib*) or *discs large 1* (*dlg1*) encoding components of the Scribble polarity module [10], and in $ras^{V12}scrib^{-}$ tumors in the eye/antennal imaginal disc (EAD) [11-13]. These results point to loss of epithelial integrity as a novel trigger of *atf3* expression and are congruent with studies linking Atf3 to processes involving transient controlled epithelial depolarization during morphogenesis and wound healing [14-16] as well as to pathological disturbances in polarity that characterize chronic wounds and tumorigenesis [5,9,17-21]. However, which polarity cues induce *atf3* expression and how Atf3 activity contributes to phenotypes associated with loss of polarity have yet to be determined.

In this study, we establish that loss of the Scrib polarity module is sufficient to increase the levels and activity of Atf3 via aPKC signaling. Increased Atf3 activity drives major phenotypic attributes of the Dlg1 deficiency as abnormal distribution of polarity proteins and differentiation defects in *dlg1* mutant epithelial clones can be alleviated by removal of Atf3. Chromatin immunoprecipitation followed by high-throughput sequencing further revealed that Atf3 target genes are enriched for roles in cytoskeletal organization and dynamics. Thus, Atf3 links defects in the Scrib polarity module with gene dysregulation and subsequent perturbations in cellular morphology and differentiation.

Results

atf3 is a cell-polarity response gene activated by aPKC but not JNK signaling

Previous transcriptome profiling by our group and others [11-13] has suggested that disturbed cell polarity leads to upregulation of *atf3* expression. Consistently, qRT-PCR from *scrib*^{1} homozygous mutant larvae and adult heads bearing *dlg1*^{G0342} homozygous mutant clones showed increased levels of *atf3* mRNA (Fig 1A), thus confirming induction of *atf3* transcription upon depletion of the Scrib polarity module. To extend this evidence, we tested whether Scrib or Dlg1 deficiency impacts the levels of an Atf3::GFP fusion protein expressed from a recombineered BAC (*atf3*^{gBAC}) that is sufficient to rescue the lethality of the *atf3*^{76} null mutants [22]. In control EAD, Atf3 was enriched in differentiated photoreceptors of the eye primordium and a subset of peripodial cells of the antenna (Fig 1B). In wing imaginal discs, Atf3::GFP protein labeled the squamous cells of the peripodial epithelium and columnar cells of the outer ring that encircles the wing pouch (Fig 1C). Knockdown of *dlg1* (*en>dlg1*^{RNAi}) or *scrib* (*en>scrib*^{RNAi}) in the posterior compartment of the wing disc resulted in a marked increase of the Atf3::GFP signal in the columnar epithelium of the wing pouch (Fig 1D, 1E). Importantly, Atf3 was also upregulated in *dlg1*^{G0342} loss-of-function mutant clones induced in the larval EAD (Fig 1F, 1G and S1A-C Fig).

Previous studies have shown that disruption of the Scrib module leads to activation of Jun-N-terminal kinase (JNK) signaling and to deregulation of the atypical protein kinase (aPKC) [23-25]. To determine if either one of these two pathways is sufficient to induce Atf3 expression, we assessed both Atf3::GFP protein levels and the activity of a synthetic Atf3-responsive element (ATRE) reporter. The ATRE construct expresses GFP or RFP under the control of four concatenated genomic segments, each of which is 22 bp long and contains an Atf3 binding site identified through ChIP-seq in this study (S1

Table, Materials and Methods). Both *in vivo* and in cultured *Drosophila* S2 cells, Atf3 activated the ATRE reporter (Fig 1M' and S2B, S2E Fig) but not its mutated version (mATRE) bearing three base pair substitutions in the Atf3 recognition sequence (S2D Fig and S1 Table). While activation of JNK signaling by expressing a wild type form of *Drosophila* JNKK (Hemipterous; Hep) induced a JNK-responsive TRE-DsRed reporter [26] (Fig 1J and S2G Fig), it failed to upregulate Atf3 expression when targeted to the posterior compartment of the wing imaginal disc (*en>hep*^{wt}) (Fig 1J''). Similarly, the ATRE-GFP reporter was insensitive to or only minimally activated by JNK signaling in the wing imaginal disc (*dpp>hep*^{wt}) and S2 cells, respectively (Fig 1N and S2E Fig). Moreover, JNK signaling appeared dispensable for Atf3 induction caused by loss of polarity, as elevated Atf3::GFP signal persisted in *dlg1* deficient EAD clones expressing a dominant negative form of the *Drosophila* JNK Basket (*dlg1*^{G0342} *bsk*^{DN}) (Fig 1H, 1I). In contrast, expression of a membrane tethered aPKC (aPKC^{CAAX}) that causes mild overgrowth was sufficient to induce both Atf3::GFP and the ATRE reporter in specified wing disc compartments (*en>aPKC*^{CAAX} and *dpp>aPKC*^{CAAX}) (Fig 1K, 1O). Although inhibiting JNK signaling suppressed the *aPKC*^{CAAX} –mediated overgrowth, it did not prevent Atf3 induction (*en>aPKC*^{CAAX} *bsk*^{DN}) (Fig 1L). Signaling via aPKC has been shown to engage Yorkie (Yki), a transcriptional co-activator in the Hippo pathway [10,27-29]. However, expression of a constitutively active form of Yorkie (*dpp>yki*^{act}) did not induce the ATRE reporter (Fig 1P). Together, these findings highlight a role for Atf3 as a polarity response gene that is activated by loss of key polarity determinants downstream of aPKC but not JNK or Yki.

Loss of *atf3* suppresses the effects of *dlg1* deficiency on eye development

Imaginal disc clones lacking either Scrib or Dlg1 surrounded by normal epithelium are severely disorganized, suffer from disturbed vesicular transport, lose the ability to terminally differentiate and

are eliminated through cell competition involving JNK signaling [23,25,30]. While JNK and its downstream transcription factor Fos are required for apoptosis and suppression of Yki-mediated hyperproliferation of *scrib* and *dlg1* mutant cells [24,25,31-34], aPKC is responsible for the aberrant morphology and differentiation of the clonal cells [23].

Because Atf3 upregulation results from depletion of the Scrib complex components as well as from ectopic aPKC activation (Fig 1D, 1E, 1K), we investigated whether this excess Atf3 might contribute to the differentiation and morphological defects of EAD clones lacking Dlg1. While EADs bearing *dlg1* deficient clones (S1B, S1C Fig) produced significantly smaller, malformed adult eyes with patches of undifferentiated tissue (Fig 2A, 2C and S3A, S3F, S3G Fig), simultaneous removal of *atf3* ($atf3^{76}dlg1^{G0342}$) (S2D, S2E Fig) almost completely restored normal eye size and morphology (Fig 2D and S3B, S3F, S3G Fig), with only minor irregularities to the orderly hexagonal lattice (Fig 2D'). An equivalent genetic interaction was observed between *atf3* and the $dlg1^{m52}$ allele [35,36] (S3D-G Fig). Importantly, adding a single copy of the $atf3^{gBAC}$ transgene to animals with the double mutant mosaic EADs ($atf3^{76}dlg1^{G0342}$;; $atf3^{gBAC}$/+) was sufficient to reinstate the aberrations to the adult eye morphology (S3C Fig), thus clearly showing that Atf3 is required for this *dlg1* deficiency phenotype to develop. Abnormalities were further exacerbated in adult eyes bearing *dlg1* deficient clones in which Atf3 was overexpressed ($dlg1^{G0342}\,atf3^{wt}$) (Fig 2E). It is important to note that mosaic overexpression of Atf3 alone disturbed the normal ommatidial arrangement in the adult eye (Fig 2F). However, immunostaining of third instar EADs against a pan-neuronal marker Elav showed that, unlike cells lacking Dlg1, Atf3-expressing clones ($atf3^{wt}$) differentiated (S2A-D Fig). In contrast, clonal loss of *atf3* alone ($atf3^{76}$) did not markedly impact adult eye morphology (Fig 2B). These data provide causal evidence for the role of Atf3 downstream of disturbed epithelial polarity. They also indicate that while Atf3 is required for

phenotypes caused by loss of *dlg1*, the gain of Atf3 alone does not fully recapitulate these defects.

Loss of *atf3* restores polarity and differentiation to *dlg1* deficient cells independent of JNK activity

Closer examination of third instar larval EADs revealed the presence of fewer $dlg1^{G0342}$ clones relative to control and $atf3^{76}$ mosaic EADs (Fig 2G-I). Many of these mutant cells showed increased activity of the JNK-responsive TRE-DsRed reporter (S5B Fig). Interestingly, simultaneous loss of *atf3* neither restored the size or abundance of $dlg1^{G0342}$ mutant cells nor prevented JNK activation (Fig 2J and S5A-C Fig). The exacerbated phenotype of $dlg1^{G0342}atf3^{wt}$ mosaic adult eyes correlated with the presence of contiguous clonal patches in third instar EAD that were markedly rounder compared to clones lacking *dlg1* alone (Fig 2I, 2K). Although the individual clones appeared larger, the overall amount of GFP positive tissue was not increased when compared to *dlg1* mutant clones (S5A Fig). The cross sections of the eye primordia further revealed that in contrast to *dlg1* deficient cells which accumulated basally, the majority of $dlg1^{G0342}atf3^{76}$ clones remained in the disc proper similar to control and *atf3* mutant cells (Fig 2M-P). Strikingly, overexpression of Atf3 in cells lacking *dlg1* promoted their apical extrusion (Fig 2Q). To rule out that clone elimination contributed to the observed rescue phenotype in the $atf3^{76}dlg1^{G0342}$ adult eyes, we took two alternative approaches. To inhibit death of clonal cells, we expressed the baculoviral caspase inhibitor p35 in $dlg1^{G0342}$ and $atf3^{76}dlg1^{G0342}$ EAD clones. To reduce competition elicited by neighboring cells, we utilized the EGUF/hid technique [37], which facilitates expression of a pro-apoptotic protein Hid in the non-clonal cells within the Glass multiple reporter (GMR) domain causing their elimination during pupal stages [38]. As expected, blocking apoptosis by p35 increased the abundance of mutant clonal cells to a similar extent in both genotypes (S5A Fig). Importantly, nearly four times more adults bearing $atf3^{76}dlg1^{G0342}p35$ mosaic EADs emerged compared to $dlg1^{G0342}p35$ animals (S5D Fig). Adult eyes derived from $dlg1^{G0342}p35$ EAD contained only small

patches of differentiated photoreceptors compared to controls (S5E, S5F Fig), whereas *atf3*^{76}*dlg1*^{G0342}*p35* eyes were either similar to those of *atf3*^{76}*dlg1*^{G0342} animals (Fig 2D and S5G Fig) or exhibited modest differentiation defects (S5H Fig). Consistently, the overall morphology and differentiation pattern was markedly improved in adult eyes composed entirely of *atf3*^{76}*dlg1*^{G0342} mutant tissue generated by the EGUF/hid method. In contrast to only remnants of differentiated tissue in *dlg1*^{G0342} mutant eyes, clear ommatidial arrays were observed in control and *atf3*^{76}*dlg1*^{G0342} adult eyes, (S5I-K Fig). Taken together, these data strongly argue against apoptosis being the basis of the genetic rescue conferred by *atf3* deficiency in *dlg1* mutant clones, and instead suggest that Atf3 contributes to cell extrusion and differentiation defects caused by loss of Dlg1.

To better characterize how loss of *atf3* impacts *dlg1* mutant phenotypes, we stained third instar larval EADs for markers of differentiation and cell adhesion. Unlike control clones, *dlg1*^{G0342} mutant cells located posterior to the morphogenetic furrow of the eye primordium frequently lacked the pan-neuronal marker Elav. Many of them flattened and delaminated, pushing some of the non-clonal Elav-positive cells to the basal side of the epithelium (Fig 3A, 3B). In contrast, *atf3*^{76}*dlg1*^{G0342} clones remain columnar, contributing to photoreceptor and interommatidial cell differentiation (Fig 3C). Importantly, immunostaining for the apical determinant Crumbs, the adherens junction protein DE-cadherin (DE-cad) and the lateral membrane marker Fasciclin III (FasIII) revealed a clear rescue of the apicobasal organization of the ommatidia in *atf3*^{76}*dlg1*^{G0342} clones compared to the disturbed architecture in clones mutant for *dlg1*^{G0342} alone (Fig 3A-F). These findings uncover novel genetic interaction between Atf3 and the central Scrib polarity module component Dlg1 and establish Atf3 as a driver of the structural and differentiation defects stemming from the loss of *dlg1.*

Disturbances to the endosomal trafficking machinery in *dlg1* mutant epithelia require Atf3

Besides altered differentiation and mislocalization of polarity proteins, disturbed cellular trafficking [30,39-41] is a hallmark feature of epithelial cells lacking the Scrib module components. Therefore, we tested if the distress of the trafficking machinery upon *dlg1* loss was Atf3-dependent. Interestingly, neither *dlg1*^{G0342} nor *atf3*^{76}*dlg1*^{G0342} EAD clones enlarged by p35 expression showed changes in the uptake of fluorescently labeled dextran compared to surrounding tissue (S6A-C Fig), indicating that endocytic activity in cells lacking *dlg1* was not affected. However, the staining of intracellular vesicle components revealed marked changes to the amount and distribution of early and recycling endosomes. While levels of the Rab5-positive vesicles (S7A Fig) were reduced in *dlg1*^{G0342} and *dlg1*^{G0342}*p35* mutants cells located in front or behind the morphogenetic furrow (Fig 4A and S8B, S8E Fig) the pool of Rab11 recycling endosomes increased (Fig 4A, 4B). In line with these findings, Dlg1-deficient cells also displayed an abnormal distribution of the Syntaxin7/Avalanche (Avl)-positive vesicles (S6E Fig). In contrast, the Rab5, Avl and Rab11 staining patterns in *atf3*^{76}*dlg1*^{G0342} double mutant EAD clones were comparable to those seen in surrounding normal tissue (Fig 4C, 4D and S6D, S6F, S7A, S7C, S7D, S7F Fig). Strikingly, the changes to the endosomal compartment observed in *dlg1* mutant tissue could be recapitulated by the Atf3 overexpression. While apical levels of Rab5 were decreased, Rab11-marked vesicles were enriched on the basal side of the wing imaginal discs in cells expressing Atf3 when compared to surrounding tissue (S8A, S8B Fig). In addition, immunostaining of wing discs bearing Atf3-expressing clones revealed changes in levels and localization of polarity proteins whose proper membrane placement requires a functional trafficking machinery [42,43]. While the apical levels of Crumbs were markedly lower, the integrin subunit Myospheroid (Mys), which normally is restricted to the basal cell surface, was detected along the entire lateral membrane in Atf3-expressing clones relative to surrounding tissue (S9C, S9D Fig). These data demonstrate that Atf3 contributes to the alterations of the endosomal machinery upon loss of polarity and its

overexpression is sufficient to mimic some of the hallmark features of *dlg1*-deficient epithelial cells. Interestingly, despite the shift in apicobasal polarity markers Atf3-expressing cells, unlike those lacking *dlg1*, maintained their columnar shape and were not extruded from the epithelium (Fig 2R and S8 Fig).

Atf3 binds a 12-nucleotide motif in genes fundamental to cytoarchitecture

As a bZIP transcription factor, Atf3 is expected to regulate gene expression through binding to specific DNA sequences. To capture a snapshot of genomic regions bound by Atf3, we employed the Atf3::GFP fusion protein expressed from the recombineered $atf3^{sBAC}$ to perform chromatin immunoprecipitation followed by high throughput sequencing (ChIP-seq). The ChIP-seq using an anti-GFP antibody identified 152 genomic locations significantly enriched in samples prepared from $atf3^{76}$;; $atf3^{sBAC}$/+ mated adult males compared to *yw* controls (Fig 5A and S1 Dataset). Using the Multiple Em for Motif Elicitation (MEME) tool [44], we derived a 12-column position weight matrix (PWM) yielding a palindromic binding site which we call the *Drosophila* Atf3 motif (Fig 5B and S2 Dataset). This motif occurred in 112 of the 152 significantly enriched peaks in Atf3 samples, which correspond to 121 genes whose *cis* regulatory regions contained an Atf3 motif (Fig 5A and S1 Dataset). Submission of this PWM to Tool for Motif to Motif comparison (TOMTOM) [45] determined that Atf3 recognizes DNA that is most similar to the Atf2 binding motif in *Drosophila* and ATF3/JDP2 motif in humans (Fig 5B). Closer examination of the Atf3-response elements revealed an 8-nucleotide core that closely resembles the cyclic AMP response element (CRE) (TGACGTCA) (Fig 5B). We have previously reported that the bZIP domain of the *Drosophila* Atf3 protein indeed directly binds this DNA element [6]. Our present experiments using the ATRE and mATRE reporters further confirm that Atf3 can control expression from this site in cultured cells and *in vivo* (Fig 1M' and S2 Fig).

The gene ontology (GO) analysis with FlyMine [46] revealed that structural and regulatory components of the cytoskeleton were significantly enriched among Atf3-bound regions. In total, 40 of the identified 121 genes containing Atf3 motifs belong to at least one out of five GO terms corresponding to cytoskeleton regulation (Fig 5A, 5C and S1 Dataset). Figure 5D depicts a summary of putative Atf3 targets engaged in their corresponding functions in a model epithelial cell. Importantly, an independent Atf3 ChIP experiment from third instar larval EADs determined that several of these targets including microtubule subunits (*alphaTub84B* and *betaTub56D*) and nuclear *Lamin C* (*LamC*) were also bound by the Atf3 in imaginal epithelia (S9A, S9B Fig) suggesting a potential mechanistic basis for the Atf3 driven phenotypes in epithelial cells with compromised apicobasal axis.

Atf3 overexpression has a broad effect on gene transcription in imaginal disc epithelia

To complement the ChIP-seq approach and characterize the transcriptional response to excess Atf3, we compared the transcriptomes of mosaic EADs overexpressing Atf3 with control expressing only GFP. Strikingly, RNA-seq revealed a widespread shift in the expression of 4957 genes (S3 Dataset), with nearly three times as many transcripts being downregulated (n = 3666) than enriched (n = 1291) by fold change ≥1.5 relative to control (Fig 5E and S3 Dataset).

Of the 121 genes identified as Atf3 targets by ChIP-seq in the adults, 32 were differentially expressed at the mRNA level (Fig 5F) in $atf3^{wt}$ mosaic EADs, most of which (23) showed transcriptional upregulation including six genes (*Arp1*, *Chd64*, *DCTN6-p27*, *Ilk*, *LamC*, *Rep*) that belonged to the cytoskeleton GO cluster (Fig 5D and 5F). In accordance with the mRNA-seq, an independent qRT-PCR of selected Atf3 ChIP-seq targets detected enrichment of *LamC*, *ude, DCTN6-p27* and *Arp1* transcripts while *alphaTub84B* and *betaTub56D* remained unchanged (S9A Fig) despite being occupied by Atf3 in both the adults and EADs (S9B Fig). To identify additional putative Atf3 targets among genes

misregulated in the RNA-seq dataset, we scanned the *Drosophila* genome with our experimentally derived Atf3 PWM using the Find Individual Motif Occurrences (FIMO) [47] and Peak Annotation and Visualization (PAVIS) [48] utilities. The Atf3 motif (Fig 5B) was found within 5 kb upstream and 1 kb downstream of 1252 genes differentially regulated in $atf3^{wt}$ mosaic EADs (Fig 5-source data 3). Importantly, a significant proportion of transcripts altered by Atf3 expression in the mosaic EADs overlapped with genes that had been found deregulated in either *scrib* or *dlg1* mutant wing imaginal discs [10] (S10 Fig and S3 Dataset). This intersection shows that the gain of Atf3 and the loss of the Scrib polarity module elicited a partly overlapping genetic response.

Atf3 controls the microtubule network and Lamin C downstream of loss of polarity

The requirement of Atf3 for the manifestation of cytoarchitecture and polarity defects in *dlg1* deficient cells prompted us to further focus on its regulation of microtubules and LamC, the primary building blocks of the cytoskeleton and nucleoskeleton, respectively. Microtubules are classically associated with controlling cell shape and division, but they are also central to polarity by serving as railroad tracks for directed vesicular trafficking [49]. Nuclear lamins on the other hand provide structure and stiffness to the nuclear envelope [50,51]. The coupling between the cytoskeleton and the nuclear lamina via the LINC- complex is essential for maintaining the mechanical properties of the cell and signal transduction [52]. Immunostaining for LamC showed that the increase in *LamC* transcription in response to excess Atf3 (Fig 5F and S9A Fig and Fig 5-source data 3) translated into a dramatic enrichment of the LamC protein in the nuclear envelope of EAD or wing disc cells overexpressing Atf3 (Fig 6A, 6D). Importantly, LamC protein levels also increased in the wing disc epithelium deficient for Scrib ($en>scrib^{RNAi}$) and in *dlg1* mutant clones of the EAD (Fig 6B, 6F), whereas they were markedly reduced in $atf3^{76}dlg1^{G0342}$ double mutant EAD clones compared to the surrounding tissue and

control clones (Fig 6C, 6E, 6G). In contrast to *LamC* enrichment, expression of multiple microtubule genes (*βTub60D*, *βTub85D* and *γTub37C*) was downregulated in *atf3*^{wt} mosaic EADs (Fig 5G, Fig 5-source data 3). Interestingly, immunostaining for α- and β-Tubulin revealed a reduced microtubule network and markedly lowered levels of non-centrosomal γ-Tubulin in Atf3-overexpressing clones of the wing imaginal disc relative to surrounding epithelial tissue (Fig 7A-C). In addition, eye primordia bearing *dlg1* mutant clones showed abnormal microtubule organization that was partially normalized by simultaneous clonal loss of *atf3* (Fig 7D-F). Taken together, our molecular and genetic approaches identified microtubule encoding genes and LamC as new targets of Atf3. We demonstrate that the upregulation of LamC and disturbances to microtubule network are the common hallmark of epithelial cells in which Atf3 activity is enhanced either by transgenic overexpression or as a result of disturbed polarity. While LamC is a *bona fide* target of Atf3, changes to microtubule network likely arise indirectly as a part of the secondary response to ectopic Atf3 activity.

Discussion

Classical insults to epithelial polarization include disruptions of the Crumbs, aPKC/Par, or Scrib protein modules, which all alter tissue organization, proliferation, differentiation, and cell viability [1]. The engagement of transcription factors presents a significant but poorly understood consequence to compromised polarity [10,23,27,28,53,54]. In this study, we identify Atf3 as a novel polarity response gene induced by aPKC signaling upon loss of the neoplastic tumor suppressors of the Scrib polarity module. We show that aPKC upregulates Atf3 independently of Yki, as increased Atf3 levels were detected in *dlg1* EAD mutant clones, where aPKC is active but Yki is functionally repressed by JNK signaling [24]. Moreover, activated Yki was not sufficient to induce Atf3 activity. Our results also exclude JNK activation stemming from loss of polarity as a driver of *atf3* expression. Blocking JNK in

dlg1 mutant clones or tissues with active aPKC signaling did not abrogate Atf3 expression. Furthermore, activation of JNK signaling neither induced Atf3 in the wing imaginal disc, nor significantly activated the ATRE reporter in S2 cells. Future studies should determine which transcription factors downstream of aPKC regulate *atf3* expression.

This study positions Atf3 as a major regulator in the aPKC circuit, as removing Atf3 from *dlg1* deficient cells recapitulated the phenotypes conferred by reduced aPKC activity in *dlg1* tissue, including restoration of a polarized, columnar morphology and differentiation in the eye primordium [23]. Importantly, Atf3 acts in a manner distinct from that of the bZIP protein Fos and the TEAD/TEF transcription factor Scalloped (Sd) and its co-activator Yki, operating downstream of disrupted polarity [23,27,28,32,54]. In *scrib* and *dlg1* mutant cells, Fos and Sd/Yki promote apoptosis and proliferation, respectively; however they are not linked to disturbed cytoarchitecture [24,27,33]. Conversely, lack of Atf3 does not block JNK activity or the elimination of *scrib*/*dlg1* mutant clones, whereas overexpression of dominant-negative forms of JNK or removal of Fos do [23,25,32]. As loss of *atf3* did not affect *dlg1* clonal abundance, we conclude that *atf3* deficiency neither reduces the proliferative potential of *dlg1* tissue nor interferes with JNK-mediated repression of Yki. Taken together, we propose that Atf3, Fos, and Sd/Yki act downstream of cell polarity insults in parallel (Fig 8).

Impairment of the vesicular trafficking machinery has been recognized as a key feature of epithelial cells lacking polarity determinants such as Crumbs or the components of the Scrib complex [30,39,41,55]. However, the deregulation of endocytosis has been also shown to drive polarity defects and to alter signal transduction resulting in overgrowth or apoptosis depending on the tissue and genetic context [30,39,41,56]. Here, we show that while bulk endocytosis is not affected in *dlg1* mutant

clonal cells of the EAD, levels and distribution of specific components of the vesicle trafficking machinery and their cargo are disturbed and these defects depend on Atf3. However, despite the clear rescue of the Rab5 and Rab11 trafficking apparatus in *atf3 dlg1* double mutant clones JNK signaling remains upregulated and cells are eliminated, suggesting that multiple mechanisms are in play to promote JNK activity upon loss of *dlg1*. Importantly, the disruption of Rab5 and Rab11-mediated trafficking routes can be recapitulated by Atf3 overexpression. The reduced levels of Crumbs, whose membrane delivery requires vesicular transport from the *trans* Golgi-network [30], and the ectopic expansion of Mys (βPS-integrin) along the lateral membrane, whose turnover relies on Rab5 and Rab21 vesicles [57] further highlight the impact of enhanced Atf3 activity on the trafficking and recycling of cellular and membrane constituents. Whether this contribution is direct or indirect via regulating cellular architecture remains to be determined.

Using unbiased ChIP-seq and RNA profiling our study provides the first *in vivo* insights into the binding specificity and transcriptional targets of *Drosophila* Atf3. The widespread transcriptional deregulation following Atf3 overexpression in epithelia indicates multiple cellular processes being affected, thus underpinning the complex phenotypes that arise in these cells. While a quarter of Atf3 ChIP-seq targets were misexpressed in $atf3^{wt}$ mosaic EADs, they represent only a fraction of all differentially regulated genes. This relatively small intersection between ChIP-seq targets identified in adult flies and the EAD transcriptome could reflect a tissue specific context for DNA-binding and transcriptional regulation by Atf3. Based on our *in silico* analysis, nearly three quarters of the genes misregulated in $atf3^{wt}$ mosaic EADs did not contain a consensus Atf3 site. It is therefore likely that the broad shift in the transcriptome profile also comprises an adaptive response to excess Atf3 activity.

Changes to the expression of microtubule genes which translate into the alterations of the microtubule cytoskeleton represent one such example.

Importantly, the transcriptional signatures of imaginal cells overexpressing Atf3 (this study) and those lacking *scrib*/*dlg1* [10] significantly overlap, which could indicate common molecular and cellular mechanisms. A novel and potentially relevant addition to this mutual genetic program is the Atf3-dependent upregulation of LamC that was elucidated through our genomic and genetic analyses. Nuclear lamins constitute the filamentous meshwork that underlies the inner nuclear membrane [50,51]. Aside from their structural role, experimental evidence links lamins to transcriptional regulation through the formation of transcriptionally repressive lamin associated domains [58]. Furthermore, the physical coupling between lamins and the cytoskeleton is critical for cytoarchitecture organization and cell polarization [59,60]. Thus, it is tempting to speculate that the direct and strong induction of *LamC* by Atf3 might have contributed to the wide shift in gene expression in EADs overexpressing Atf3 and/or disturbances in the microtubule network and cell polarity. However, clonal expression of a LamC transgene was insufficient to mimic defects of Atf3 overexpression or *dlg1* loss (S11 Fig), underscoring the unlikely capacity of any single target gene to recapitulate phenotypes of Atf3 gain.

Finally, it is important to note that the extent of Atf3 activity and the signaling milieu differ between *dlg1* mutant epithelia and cells overexpressing Atf3, and therefore the two conditions cannot be expected to phenocopy each other. The model presented in Figure 8 summarizes the shared and distinct roles of Atf3 in these contexts as established in this study.

Outlook

A growing body of evidence points to striking similarities in the cellular and molecular events underlying loss of polarity and wounding [10,61]. In this context, the induction of Atf3 upon loss of polarity is in line with the early discovery of *ATF3* as a gene rapidly induced in the regenerating rat liver [62] and recent studies showing Atf3 induction during epithelial wounding [15,16]. Here we demonstrate that Atf3 levels remain low as long as epithelial polarity is intact, whereas loss of polarity due to deficiency in tumor suppressors of the Scrib complex triggers Atf3 expression. Future investigations into the link between *Drosophila* Atf3 and cell polarity are likely to unravel the impact of ATF3 expression on epithelial homeostasis and on human pathologies arising from polarity breakdown.

MATERIALS AND METHODS

Flies

The following fly strains were used: (a) *y* w^{1118},(b) w^{1118},(c) *y* $atf3^{76}$ *w/FM7i, P{ActGFP}JMR3* [6], (d) $atf3^{gBAC}$ [22], (e) *en-GAL4* (RRID: BDSC_30564), (f) *dpp-GAL4* (RRID: BDSC_7007), (g) *UAS-*$atf3^{V}$ (this study as $atf3^{wt}$) [6], (h) *hsFLP; act>*y^{+}*>GAL4, UAS-GFP*, (i) *hsFLP; act>*y^{+}*>GAL4, UAS-GFP, UAS-*$atf3^{wt}$ (this study), (j) *FRT19A* (RRID: BDSC_1744), (k) *FRT82B* (RRID: BDSC_5619), (l) *UAS-p35/CyO* (RRID: BDSC_5072), (m) *GMR-hid y w FRT19; ey-Gal4, UAS-FLP* (RRID: BDSC_5248), (n) *FRT19A* $dlg1^{G0342}$ (111872, DGRC), (o) $dlg1^{m52}$ (a generous gift from F. Papagiannouli), (p) *FRT82B* $scrib^{1}$ [25], (q) *eyFLP FRT19A tubGAL80; act>*y^{+}*>GAL4, UAS*-GFP (this study), (r) *eyFLP FRT19A, tubGAL80; act>*y^{+}*>GAL4, UAS-myrRFP* (this study), (s) *eyFLP; act>*y^{+}*>GAL4, UAS-GFP; FRT82B, tubGAL80* [63], (t) *UAS-*$dlg1^{RNAi}$ (41134, VDRC), (u) *UAS-*$scrib^{RNAi}$ (105412, VDRC), (v) *TRE-DsRed* (attP16) [26], (w) *UAS-*hep^{wt}, (x) *UAS-*$yki^{S111A.S168A.S250A.V5}$ (RRID: BDSC_28817, this study as yki^{act}), (y) *UAS-mCD8-ChRFP* (RRID:BDSC_27391, this study as *UAS-mCherry*), (z)*UAS-*$aPKC^{CAAX}$ [64], (aa) *UAS-LamC* [65], (bb) *UAS-*bsk^{DN}. A transgenic

ATRE-GFP line was obtained using the attP16 landing site [66]. The *atf3*^{gBAC} fly line was used for immunostaining of Atf3::GFP. For detailed descriptions of fly crosses, see S2 Table. All crosses were carried out at 25 °C unless stated otherwise.

Quantitative reverse transcription-PCR (qRT-PCR)

For each biological replicate, total RNA was isolated from 10 larvae or 15 adult heads with Isol-RNA Lysis Reagent (5 Prime). After DNase I treatment (Ambion, Foster City, CA), cDNA was synthesized from 1μg of RNA using oligo(dT) primers and Superscript III (Life Technologies). PCR was performed in triplicate with BioRad 2x SYBR Green mix in the CFX96 real-time PCR system (Bio-Rad, Hercules, CA). All primers were designed to anneal at 62 °C (see S1 Table for oligonucleotide sequences). All data were normalized to *rp49* transcript levels, and fold changes in gene expression were calculated using the $\Delta\Delta C_T$ method [67].

Genetic mosaic analysis

Clones expressing *atf3* in the wing imaginal disc were generated using a *hsFLPout* method described in [6]. Crosses were kept at 22 °C. Four days after egg lay, progeny were heat shocked for 30 min in a 37 °C water bath. Imaginal discs were dissected from wandering third instar larvae. Generation of mosaics in EADs using Mosaic Analysis with a Repressible Cell Marker method (MARCM) [68] was carried out as described [32].

ChIP-seq

For each genotype (see S2 Table), three biological ChIP replicates and one input replicate were generated. For each ChIP replicate, 1.2 g of adult males were collected and processed using a modified version of the protocol described in [69]. Anesthetized males were split into two batches of 600 mg and flash frozen using liquid nitrogen, pulverized with a mortar and pestle, and disrupted further via

20 strokes of a loose fitting pestle in a Dounce homogenizer containing 10 ml of Crosslinking Solution (1 mM EDTA, 0.5 mM EGTA, 100 mM NaCl, 50 mM HEPES, pH 8.0) supplemented with proteases inhibitors (11873580001, Roche). The remainder of the protocol describes the processing of a single batch. The suspension was centrifuged for 1 min at 400 g in a swing bucket rotor and then passed through two layers of 64 μm Nitex membrane into a 15 ml Falcon tube. To crosslink Atf3 to chromatin, formaldehyde was added to a final concentration of 1.8% to the Falcon tube containing 10 ml of cleared fly homogenate. The Falcon tube was then incubated on an orbital shaker at room temperature for 10 min. Crosslinking was stopped by adding glycine to a final concentration of 225 mM and shaking for a further 5 min. After centrifugation for 10 min at 1,100 g in a swing bucket rotor, cells were resuspended in 10 ml of Cell Lysis Buffer (85 mM KCl, 0.5% IGEPAL CA-630 (v/v), 5 mM HEPES, pH 8.0) supplemented with protease inhibitors and lysed in a Dounce homogenizer via twenty strokes with a tight fitting pestle. Nuclei were pelleted at 2000 g for 4 min and washed in 5 ml of Cell Lysis Buffer three times. Nuclei were resuspended in 2 ml of TBS Lysis Buffer (50 mM Tris-Cl pH 7.8, 150 mM NaCl, 1 mM EDTA pH 8.0, 1% Triton-X100, 0.01% IGEPAL CA-630) supplemented with protease inhibitors and incubated for 10 min on an orbital shaker. While submerged in an ice water bath, chromatin was sheared to 300-500 bp fragments by applying fifty 30 seconds on/30 seconds off cycles of a Branson 250 microtip sonifier with Output set to 3.5 and Duty Cycle set to 50%. The 2 ml of chromatin was split equally into two 1.5 ml low binding microcentrifuge tubes (710176, Biozym). Debris was cleared from the chromatin by centrifugation at 20,000 g for 10 min. Chromatin was cleared overnight in two tubes at 4 °C by the addition of 40 μl of sepharose-IgG beads (17-0969-01,GE) equilibrated in TBS Lysis Buffer. 100 μl of cleared chromatin was retained as an INPUT sample for sequencing. Remaining cleared chromatin was transferred to two new low binding tubes and precipitated overnight at 4 °C with 40 μl GFP Trap beads (gta-20, Chromotek) per tube. Beads were

washed 5 times with cold TBS Lysis Buffer supplemented with protease inhibitors. From this point on, the beads and INPUT sample retained earlier were processed in the same fashion. Samples were resuspended in 100 μl TE buffer (1 mM EDTA, 10 mM Tris-HCl, pH 8.0) supplemented with 50 μg/ml RNase A, transferred to PCR tubes, and incubated in a thermal cycler with heated lid at 37 °C for 30 min. SDS was added to a final concentration of 0.5% (w/v) from a 10% stock proteinase K to a final concentration of 0.5 mg/ml. Tubes were then incubated at 37 °C for 12 hours followed by 65 °C for 6 h in a thermal cycler with heated lid to partially reverse the crosslinks. H_2O was added to a final volume of 200 μl, and DNA was purified by phenol:chloroform extraction. DNA was ethanol precipitated in a low binding 1.5 ml microcentrifuge tube with sodium acetate and glycogen. DNA was washed once with 70% ethanol. DNA pellets derived from the original 1.2 g of starting adult fly material (4 microcentrifuge tubes in the end) were resuspended in 15 μl of TE.

Sequencing libraries were generated from input and ChIP samples according to the Illumina protocol for total ChIP-seq library preparation. All samples were loaded onto a single Illumina flow cell (Illumina, San Diego, CA). Using the Illumina HiSeq 2000 instrument, 50 bp of sequence were read from one DNA end. Image analysis and base calling were done with the Illumina RTA software (RRID: SCR_014332) at run time. Sequences were mapped to the *Drosophila* genome assembly (version BDGP R5/dm3, April 2006) and delivered as BAM files.

DNA motif analyses

To identify regions bound by Atf3, BEDTools [70] (RRID: SCR_006646) was used to convert BAM files from Atf3 and control samples (3 biological ChIP replicates and one input sample each) into BED files, which were subsequently submitted to a Comparative Profile Analyzer (CoPrA) workflow to call and test the statistical significance of differentially enriched genomic locations in Atf3 ChIP-seq samples

relative to control. The differential analysis depends on base-resolution coverage profiles of the Atf3 and control ChIP samples as well as the input data from both samples. They were generated from uniquely mapped reads that were extended to the original fragment length of 200 bp resulting in 6 ChIP and 2 input coverage profiles. All profiles are normalized through division of the base-wise coverage values by the total number of respective sample reads multiplied by one Million. Thereby normalized input profiles from Atf3 and control samples are subtracted from normalized Atf3 and control ChIP-profile replicates, respectively. Every processed ChIP profile replicate is then scaled separately to transform its values into the range [0,1]. They were then discretized by calculating the coverage mean of a defined sliding window. Since transcription factor binding peaks cover a small region on the genome, its size was adjusted to 50 bp. The shift is set by default to half of the window size. In the next step the discretized replicate profiles of the same sample type are combined to one resulting discretized profile by taking the mean of the window values at the same genomic position respectively. The thus processed sample profiles of Atf3 and control are finally utilized to generate a difference profile by taking the Euclidean difference between Atf3 and control values at the same genomic position. The obtained values of the difference profile are normally distributed and are located between -1 and 1 with a mean very close to 0. To filter out non-informative difference regions the profile is cleaned by removing all values within the range of 4 times the standard deviation of the mean. Remaining difference regions which are adjacent to each other and that possess the same sign are merged. They either show enrichment for Atf3 or control. They are size filtered by taking the discretization window size as a minimal threshold. The resulting difference regions are finally tested for significance by a two-sided Kolmogorov-Smirnov test of the discretized region values of Atf3 and control and multiple testing corrected by Benjamini-Hochberg. We accepted differential regions with a q-value < 0.05 that are enriched in the Atf3 sample and extracted their DNA sequences with BEDTools.

Peaks were assigned to genes when located within a gene or 1 kb upstream of the transcriptional start site. Multiple genes were manually associated with a peak in the case of nested genes or dense gene regions. Enriched regions mapping to positions within the CH321-51N24 BAC (source of the *atf3*^{gBAC}) were discarded (n=59), except for two peaks corresponding to the genes *atf3* and *CG11403*, which contained the *Drosophila* Atf3 motif.

Sequences of regions bound by Atf3 were uploaded to MEME (http://meme.nbcr.net/meme/cgi-bin/meme.cgi) for motif identification [44]. The positional weight matrix returned by MEME was submitted to TOMTOM (http://meme.nbcr.net/meme/cgi-bin/tomtom.cgi) for interspecies motif comparison [45]. FlyBase gene ontology (GO) terms identified with FlyMine (http://www.flymine.org, RRID: SCR_002694) were used for functional annotation [46].

ChIP from eye/antennal imaginal discs

A custom protocol combining the methods described in [69,71] was used to perform ChIP against Atf3 in the EADs. For each replicate, 100 EADs with mouth hooks attached were dissected from third instar larvae in ice-cold PBS. Discs were fixed at room temperature by gently mixing in 1 ml cross-linking solution (1.8% formaldehyde, 50 mM Hepes pH 8.0, 1 mM EDTA, 0.5 mM EGTA, 100 mM NaCl), which was changed 3-4 times during fixation. Fixation was stopped by washing for 3 min in 1 ml PBS/0.01% Triton X-100/125 mM glycine 3-4 times. Fixed discs were washed for 10 min in 1 ml wash A (10 mM Hepes pH 7.6, 10 mM EDTA, 0.5 mM EGTA, 0.25% Triton X-100) and subsequently for 10 min in 1 ml wash B (10 mM Hepes pH 7.6, 200 mM NaCl, 1 mM EDTA, 0.5 mM EGTA, 0.01% Triton X-100), with the wash solutions being changed 3-4 times over the 10 min. Eye discs were separated from the brain and mouth hooks and transferred into 550 μl of TBS Lysis Buffer (see ChIP-seq protocol). Chromatin was sheared using an Active Motif EpiShear sonicator (Active Motif, 53052) equipped with

a 1.5 ml EpiShear Cooled Sonication Platform (Active Motif, 53080) and 1.5 ml Benchtop Cooler (Active Motif, 53076). With Amplitude set to 50%, sonication was performed in cycles of 20 seconds on/30 seconds off for 20 minutes. Chromatin was centrifuged at 14,000 RPM for 10 min to clear debris, transferred into clean 1.5 ml tubes, and cleared overnight at 4 °C with 20 µl sepharose-IgG beads equilibrated in TBS Lysis Buffer. Cleared chromatin was transferred to new 1.5 ml tubes and precipitated overnight at 4 °C with 25 µl GFP Trap beads per tube. Beads were washed the indicated number of times with 1 ml of each of the following buffers at 4 °C on a rotating wheel for 10 min: 1 × TBS Lysis Buffer , 4 × TBS 500 Lysis Buffer (50 mM Tris-Cl pH 7.8, 500 mM NaCl, 1 mM EDTA pH 8.0, 1% Triton-X100, 0.01% IGEPAL CA-630), 1x LiCl buffer (250 mM LiCl, 1 mM EDTA, 0.5% IGEPAL CA-630 (v/v), 10 mM Tris-HCl, pH 8.0). Beads were transferred into clean 1.5 ml tubes and washed 2 × with TE for 10 min at 4 °C on a rotating wheel. Beads were subsequently transferred into PCR tubes. Chromatin was decrosslinked and precipitated as described in the ChIP-seq protocol. Purified DNA was raised in 500 µl water.

qPCR was performed in triplicate with BioRad 2x SYBR Green mix in the CFX96 real-time PCR system (Bio-Rad, Hercules, CA). All primers were designed to anneal at 62 °C (see S1 Table 1 for oligonucleotide sequences). Data were normalized to amplification values for *ecd*. Fold enrichment of chromatin was calculated using the $\Delta\Delta C_T$ method [67].

RNA-seq

RNA was isolated from *FRT82B atf3*^{wt} mosaic EADs of third instar larvae as described [72]. Total RNA libraries were generated according to the Illumina protocol and single-end sequenced on an Illumina NextSeq 500 instrument at 75 bp read length. Image analysis and base calling were done with the Illumina RTA software at run time. Published sequence data from *FRT82B* mosaic EAD samples [11]

were used as control. Data were processed using a high-throughput Next-Generation Sequencing analysis pipeline [73]. Basic read quality check was performed with FastQC (v0.10.1) (RRID: SCR_014583) and read statistics were acquired with SAMtools v0.1.19 (RRID: SCR_002105) [74]. Reads were mapped to the *Drosophila* reference assembly (version BDGP R5/dm3, April 2006) using Tophat v2.0.10 (RRID: SCR_013035) [75], and gene quantification was carried out using a combination of Cufflinks v2.1.1 (RRID: SCR_014597) [76], and the DESeq2 package v1.10.1 (RRID: SCR_000154) [77], with genomic annotation from the Ensembl database (RRID: SCR_002344), version 84. In all samples, the number of total reads exceeded 50 million, from which an average 83.6 percent could be mapped, and on average 97.5% of these mapped reads fulfilled the MAPQ≥30 criterion. The results were uploaded into an in-house MySQL database and joined with BiomaRt (RRID: SCR_002987) v2.26.1 [78] annotations from Ensembl, version 84. Lists of differentially expressed genes were defined by a final database export using 5 and 0.01 as cutoffs for DESeq2-based FCs and p-values, respectively. To identify genes differentially expressed under the respective conditions, the average of at least three biological replicates was calculated. Figure 5-source data 1 shows all transcripts whose expression differed ≥ 1.5-fold in *FRT82B atf3*^{wt} compared to *FRT82B* control.

Atf3 motif search

The experimentally derived *Drosophila* Atf3 PWM was submitted to the online FIMO utility (http://meme-suite.org/tools/fimo) (RRID: SCR_001783) to identify Atf3 motifs in *Drosophila melanogaster* genome (UCSC, dm3), with a p-value threshold set at 0.0001. FIMO results, in the form of a BED file, were subsequently submitted to the online PAVIS tool (http://manticore.niehs.nih.gov/pavis3), using default settings.

Plasmid constructs

To create the Atf3 expression reporter, oligonucleotides containing four intact or mutated Atf3 sites (see S1 Table for sequences) were cloned via Mlu1 and Not1 sites into the pRedRabbit and pGreenRabbit vectors [79]. To express N-terminally tagged GFP- or FLAG-Atf3 proteins from the UAST promoter, *atf3* cDNA (see S1 Table for oligonucleotide sequences) was cloned into pENTR4 and subsequently recombined using LR Clonase II (11791-020, Life Technologies) into pTGW and pTFW vectors, respectively (T. Murphy, *Drosophila* Genomic Resource Center).

S2 cell culture

Schneider 2 (S2) cells were cultured at 25 °C in Shields and Sang M3 insect medium (S8398-1L, Sigma-Aldrich) containing 8% fetal bovine serum (Gibco, Life Technologies) without antibiotics. Cells were transfected using X-tremeGENE (Roche Applied Science). Expression of UAS-driven genes was induced by co-transfection with a pWA-GAL4 plasmid expressing GAL4 under an *actin5C* promoter (a gift from Y. Hiromi). Cells were fed 24 hours after transfection. Cells were imaged or lysed 72 hours after transfection.

Tissue staining

Tissues from third instar larvae were processed as described previously [6]. The following primary and secondary antibodies were used at the indicated dilutions: anti-Dlg1 (RRID: AB_528203; 1:200), anti-Fasciclin III (RRID: AB_528238; 1:200), anti-Elav (RRID: AB_528217 and AB_528217; 1:200), anti-DE-cad (RRID: AB_528120; 1:200), anti-Crumbs (RRID: AB_528181; 1:200), anti-p120-catenin (RRID: AB_2088073; 1:200), anti-α–Tubulin (RRID: AB_579793; 1:200), anti-β–Tubulin (RRID: AB_2315513; 1:200), anti-LaminC (RRID: AB_528339; 1:500) and anti-βPS integrin (RRID: AB_528310; 1:200) from the Developmental Studies Hybridoma Bank (DSHB) (Iowa City, Iowa), rabbit-anti γ-tubulin (T6557, Sigma Aldrich; 1:50), rabbit anti-GFP (G10362, Invitrogen; 1:500), rabbit-anti-Rab5 (ab31261, Abcam;

1:200), mouse-anti-Rab11 (BD610656, BD Biosciences; 1:200), chicken-anti-Avl (a gift from D. Bilder, 1:500) and Cy2, Cy3- and Cy5-conjugated secondary antibodies (Jackson Immunoresearch). Tissues were counterstained with DAPI (1 μg/ml) and mounted in DABCO-Mowiol medium (Sigma-Aldrich).

Dextran uptake assay

Third instar imaginal discs were incubated in M3 media containing 0.5 mM MW3000 Texas Red dextran (D3328; ThermoFisher Scientifc) for 15 minutes (pulse) at 25 °C. Discs were briefly washed 2 times in M3 media followed by incubation in M3 media for 60 minutes (chase). Discs were subsequently fixed in PBS-1% formaldehyde for 20 min, counterstained with DAPI, and mounted in DABCO-Mowiol medium (Sigma-Aldrich).

Image acquisition and processing

S2 cells were imaged using a DP72 camera mounted on an Olympus CK4X41 miscroscope, in conjunction with cellSens 1.1 Software (RRID: SCR_014551). Confocal images were acquired at room temperature using an Olympus FV1000 confocal microscope equipped with 20x UPlan S-Apo (NA 0.85), 40x UPlan FL (NA 1.30) and 60x UPlanApo (NA 1.35) objectives. Transversal sections were generated using Imaris 7.0.0 (Bitplane) (RRID: SCR_007370). Figure assembly and image brightness and contrast adjustments were done in Photoshop CS5.1 (Adobe Systems, Inc.) (RRID: SCR_014199). Z-stacks of adult eyes were taken using a motorized Leica M165 FC fluorescent stereomicroscope equipped with the DFC490 CCD camera. Images were processed using the Multifocus module of LAS 3.7.0 software (Leica).

Flow cytometry of eye/antenna imaginal discs

Third instar larvae were collected and washed 2x with PBS. EADs were dissected in PBS (on average sixty EADs /replicate/genotype) and transferred to 1.5 ml low binding microcentrifuge tubes (no more

than one hour before dissociation). PBS was removed from EADs and was replaced with 100 μl dissociation solution containing 1 mg/ml collagenase I (Sigma, C2674), and 1 mg/ml papain (Sigma P4762). Samples were incubated for 60 min at room temperature and gently swirled every 15 min. After the dissociation solution was removed, discs were carefully rinsed with 500 μl PBS, which was then replaced with 100 μl of PBS. The final dissociation was performed by passing the discs through a 27G insulin syringe (Terumo) five times. Additional 200 μl of PBS was added for a final volume of 300 μl (5 μl PBS per disc). Following sample filtration through a Filcone filter, propidium iodide was added to measure cell viability and samples were stored on ice until sorting. For each sample (n≥3 per genotype), 30,000 events were counted on a BD LSRFortessa Cell Analyzer in combination with BD FACSDiva software v8.0 (both BD Bioscience) using gates set to distinguish GFP+, GFP-, and PI- cells.

Scanning electron microscopy

Adult heads were fixed in 80% ethanol, postfixed with 1% osmium tetroxide, dehydrated in ethanol, critical point dried, gold coated, and observed under a JEOL JSM-7401F (Tokyo, Japan) 6300 scanning electron microscope.

Immunoblotting

S2 cells were lysed in 50 mM Tris-HCl (pH 7.8), 150 mM NaCl, 1 mM EDTA (pH 8.0), 1% Triton X-100, 0.01% Igepal, and protease inhibitors (Roche Applied Science). Protein concentration was quantified using Pierce 660 reagent (22660, Thermo Scientific) according to manufacturer's instructions. Following SDS-PAGE, proteins were detected by immunoblotting with mouse anti-Flag M2 (1:1000, Sigma Aldrich), rabbit anti-GFP (1:5000, TP401, Acris) and mouse anti-α-Spectrin (1:1000, RRID: AB_528473) antibodies, followed by incubation with corresponding HRP-conjugated secondary antibodies (Jackson Immuno Research). Chemiluminescent signal was captured using ImageQuant

LAS4000 reader (GE Healthcare).

Sample Size Criteria

For sample size criteria, *post hoc* analysis of results presented in Figs 1, S1, S3, S5 and S9 using G*Power 3.1 (RRID: SCR_013726) [80] determined that the statistical power of all statistically significant differences (1-β) exceeded 0.94, given sample size, mean, and standard deviation for each condition.

Acknowledgements

We thank Dirk Bohmann, Sarah Bray, Sonsoles Campuzano, Fani Papagiannouli, Andreas Wodarz, Lori Wallrath, David Bilder, the Bloomington Stock Center (Bloomington, USA), the Vienna *Drosophila* Resource Center (VDRC, Vienna, Austria), NIG-Fly Stock Center (Mishima, Japan), the Developmental Studies Hybridoma Bank (DSHB, Iowa, USA) and the *Drosophila* Genomics Resource Center (Bloomington, USA) for plasmids, fly stocks, and antibodies. We are grateful to Alvaro Rada-Iglesias for advice on ChIP, Vladimir Benes and the Genomics Core Facility in EMBL for ChIP and mRNA sequencing and Peter Frommolt and Prerana Wagle from the CECAD Bioinformatics Facility Cologne for mRNA-seq data processing, and Merve Kilinc for assistance with FACS. We acknowledge the Laboratory of Electron Microscopy (Biology Center, CAS), supported by the Czech-BioImaging large RI project LM2015062. We thank Tina Bresser and Nils Teuscher for technical assistance.

References

1. Tepass U. The Apical Polarity Protein Network in Drosophila Epithelial Cells: Regulation of Polarity, Junctions, Morphogenesis, Cell Growth, and Survival. Annu Rev Cell Dev Biol. Annual Reviews; 2012;28: 655–685.

2. Kockel L, Homsy JG, Bohmann D. Drosophila AP-1: lessons from an invertebrate. Oncogene. Nature Publishing Group; 2001;20: 2347–2364. doi:10.1038/sj.onc.1204300

3. Angel P, Szabowski A, Schorpp-Kistner M. Function and regulation of AP-1 subunits in skin physiology and pathology. Oncogene. 2001;20: 2413–2423. doi:10.1038/sj.onc.1204380

4. Zenz R, Scheuch H, Martin P, Frank C, Eferl R, Kenner L, et al. c-Jun Regulates Eyelid Closure and Skin Tumor Development through EGFR Signaling. Developmental Cell. 2003;4: 879–889. doi:10.1016/S1534-5807(03)00161-8

5. Wang A, Arantes S, Conti C, McArthur M, Aldaz CM, Macleod MC. Epidermal hyperplasia and oral carcinoma in mice overexpressing the transcription factor ATF3 in basal epithelial cells. Mol Carcinog. Wiley Subscription Services, Inc., A Wiley Company; 2007;46: 476–487. doi:10.1002/mc.20298

6. Sekyrova P, Bohmann D, Jindra M, Uhlirova M. Interaction between Drosophila bZIP proteins Atf3 and Jun prevents replacement of epithelial cells during metamorphosis. Development. 2010;137: 141–150. doi:10.1242/dev.037861

7. Hai T, Wolford CC, Chang Y-S. ATF3, a hub of the cellular adaptive-response network, in the pathogenesis of diseases: is modulation of inflammation a unifying component? gene expr. 2010;15: 1–11. doi:10.3727/105221610X12819686555015

8. Kool J, Hamdi M, Cornelissen-Steijger P, van der Eb AJ, Terleth C, van Dam H. Induction of ATF3 by ionizing radiation is mediated via a signaling pathway that includes ATM, Nibrin1, stress-induced MAPkinases and ATF-2. Oncogene. 2003;22: 4235–4242. doi:10.1038/sj.onc.1206611

9. Wu X, Nguyen B-C, Dziunycz P, Chang S, Brooks Y, Lefort K, et al. Opposing roles for calcineurin and ATF3 in squamous skin cancer. Nature. 2010;465: 368–372. doi:10.1038/nature08996

10. Bunker BD, Nellimoottil TT, Boileau RM, Classen AK, Bilder D, McNeill H. The transcriptional response to tumorigenic polarity loss in Drosophila. eLife. eLife Sciences Publications Limited; 2015;4: e03189. doi:10.7554/eLife.03189

11. Külshammer E, Mundorf J, Kilinc M, Frommolt P, Wagle P, Uhlirova M. Interplay among Drosophila transcription factors Ets21c, Fos and Ftz-F1 drives JNK-mediated tumor malignancy. Dis Model Mech. Company of Biologists; 2015;8: 1279–1293. doi:10.1242/dmm.020719

12. Atkins M, Potier D, Romanelli L, Jacobs J, Mach J, Hamaratoglu F, et al. An Ectopic Network of Transcription Factors Regulated by Hippo Signaling Drives Growth and Invasion of a Malignant Tumor Model. Curr Biol. 2016;26: 2101–2113. doi:10.1016/j.cub.2016.06.035

13. Doggett K, Turkel N, Willoughby LF, Ellul J, Murray MJ, Richardson HE, et al. BTB-Zinc Finger Oncogenes Are Required for Ras and Notch-Driven Tumorigenesis in Drosophila. Bergmann A, editor. PLoS ONE. Public Library of Science; 2015;10: e0132987. doi:10.1371/journal.pone.0132987

14. Sekyrova P, Bohmann D, Jindra M, Uhlirova M. Interaction between Drosophila bZIP proteins Atf3 and Jun prevents replacement of epithelial cells during metamorphosis. Development.

Oxford University Press for The Company of Biologists Limited; 2010;137: 141–150. doi:10.1242/dev.037861

15. Harper EG, Alvares SM, Carter WG. Wounding activates p38 map kinase and activation transcription factor 3 in leading keratinocytes. Journal of Cell science. 2005;118: 3471–3485. doi:10.1242/jcs.02475

16. Khan SJ, Abidi SNF, Skinner A, Tian Y, Smith-Bolton RK. The Drosophila Duox maturation factor is a key component of a positive feedback loop that sustains regeneration signaling. Bosco G, editor. PLoS Genet. Public Library of Science; 2017;13: e1006937. doi:10.1371/journal.pgen.1006937

17. Wang A, Arantes S, Yan L, Kiguchi K, McArthur MJ, Sahin A, et al. The transcription factor ATF3 acts as an oncogene in mouse mammary tumorigenesis. BMC Cancer. 2008;8: 268. doi:10.1186/1471-2407-8-268

18. Pastar I, Stojadinovic O, Krzyzanowska A, Barrientos S, Stuelten C, Zimmerman K, et al. Attenuation of the Transforming Growth Factor β –Signaling Pathway in Chronic Venous Ulcers. Molecular Medicine. The Feinstein Institute for Medical Research; 2010;16: 92–101. doi:10.2119/molmed.2009.00149

19. Pelzer AE, Bektic J, Haag P, Berger AP, Pycha A, Schäfer G, et al. The Expression of Transcription Factor Activating Transcription Factor 3 in the Human Prostate and its Regulation by Androgen in Prostate Cancer. The Journal of Urology. 2006;175: 1517–1522. doi:10.1016/S0022-5347(05)00651-8

20. Yuan X, Yu L, Li J, Xie G, Rong T, Zhang L, et al. ATF3 Suppresses Metastasis of Bladder Cancer by Regulating Gelsolin-Mediated Remodeling of the Actin Cytoskeleton. Cancer Res. 2013;73: 3625–3637. doi:10.1158/0008-5472.CAN-12-3879

21. Yin X, Dewille JW, Hai T. A potential dichotomous role of ATF3, an adaptive-response gene, in cancer development. Oncogene. 2008;27: 2118–2127. doi:10.1038/sj.onc.1210861

22. Rynes J, Donohoe CD, Frommolt P, Brodesser S, Jindra M, Uhlirova M. Activating Transcription Factor 3 Regulates Immune and Metabolic Homeostasis. Mol Cell Biol. 2012;32: 3949–3962. doi:10.1128/MCB.00429-12

23. Leong GR, Goulding KR, Amin N, Richardson HE, Brumby AM. Scribble mutants promote aPKC and JNK-dependent epithelial neoplasia independently of Crumbs. BMC Biol. 2009;7: 62. doi:10.1186/1741-7007-7-62

24. Chen CL, Schroeder MC, Kango-Singh M, Tao C, Halder G. Tumor suppression by cell competition through regulation of the Hippo pathway. 2012;109: 484–489. doi:10.1073/pnas.1113882109

25. Brumby AM, Richardson HE. scribble mutants cooperate with oncogenic Ras or Notch to cause neoplastic overgrowth in Drosophila. EMBO J. 2003;22: 5769–5779. doi:10.1093/emboj/cdg548

26. Chatterjee N, Bohmann D. A versatile ΦC31 based reporter system for measuring AP-1 and Nrf2

signaling in Drosophila and in tissue culture. PLoS ONE. 2012;7: e34063. doi:10.1371/journal.pone.0034063

27. Doggett K, Grusche FA, Richardson HE, Brumby AM. Loss of the Drosophila cell polarity regulator Scribbled promotes epithelial tissue overgrowth and cooperation with oncogenic Ras-Raf through impaired Hippo pathway signaling. BMC Dev Biol. 2011;11: 57. doi:10.1186/1471-213X-11-57

28. Grzeschik NA, Parsons LM, Allott ML, Harvey KF, Richardson HE. Lgl, aPKC, and Crumbs Regulate the Salvador/Warts/Hippo Pathway through Two Distinct Mechanisms. Current Biology. 2010;20: 573–581. doi:10.1016/j.cub.2010.01.055

29. Yang C-C, Graves HK, Moya IM, Tao C, Hamaratoglu F, Gladden AB, et al. Differential regulation of the Hippo pathway by adherens junctions and apical–basal cell polarity modules. 2015;112: 1785–1790. doi:10.1073/pnas.1420850112

30. de Vreede G, Schoenfeld JD, Windler SL, Morrison H, Lu H, Bilder D. The Scribble module regulates retromer-dependent endocytic trafficking during epithelial polarization. Development. Oxford University Press for The Company of Biologists Limited; 2014;141: 2796–2802. doi:10.1242/dev.105403

31. Igaki T, Pagliarini RA, Xu T. Loss of cell polarity drives tumor growth and invasion through JNK activation in Drosophila. Curr Biol. 2006;16: 1139–1146. doi:10.1016/j.cub.2006.04.042

32. Uhlirova M, Jasper H, Bohmann D. Non-cell-autonomous induction of tissue overgrowth by JNK/Ras cooperation in a Drosophila tumor model. 2005;102: 13123–13128. doi:10.1073/pnas.0504170102

33. Uhlirova M, Bohmann D. JNK- and Fos-regulated Mmp1 expression cooperates with Ras to induce invasive tumors in Drosophila. EMBO J. 2006;25: 5294–5304. doi:10.1038/sj.emboj.7601401

34. Ohsawa S, Sugimura K, Takino K, Xu T, Miyawaki A, Igaki T. Elimination of oncogenic neighbors by JNK-mediated engulfment in Drosophila. 2011;20: 315–328. doi:10.1016/j.devcel.2011.02.007

35. Woods DF, Bryant PJ. Molecular cloning of the lethal(1)discs large-1 oncogene of Drosophila. Dev Biol. 1989;134: 222–235.

36. Perrimon N. The maternal effect of lethal(1)discs-large-1: A recessive oncogene of Drosophila melanogaster. Dev Biol. 1988;127: 392–407.

37. Stowers RS, Schwarz TL. A genetic method for generating Drosophila eyes composed exclusively of mitotic clones of a single genotype. Genetics. 1999;152: 1631–1639.

38. Fan Y, Bergmann A. Multiple Mechanisms Modulate Distinct Cellular Susceptibilities toward Apoptosis in the Developing Drosophila Eye. Developmental Cell. Elsevier Inc; 2014;30: 48–60. doi:10.1016/j.devcel.2014.05.007

39. Igaki T, Pastor-Pareja JC, Aonuma H, Miura M, Xu T. Intrinsic tumor suppression and epithelial

maintenance by endocytic activation of Eiger/TNF signaling in Drosophila. 2009;16: 458–465. doi:10.1016/j.devcel.2009.01.002

40. Lohia M, Qin Y, Macara IG. The Scribble Polarity Protein Stabilizes E-Cadherin/p120-Catenin Binding and Blocks Retrieval of E-Cadherin to the Golgi. Gottardi C, editor. PLoS ONE. Public Library of Science; 2012;7: e51130. doi:10.1371/journal.pone.0051130

41. Parsons LM, Portela M, Grzeschik NA, Richardson HE. Lgl regulates Notch signaling via endocytosis, independently of the apical aPKC-Par6-Baz polarity complex. Curr Biol. 2014;24: 2073–2084. doi:10.1016/j.cub.2014.07.075

42. Nelson WJ. Remodeling Epithelial Cell Organization: Transitions Between Front–Rear and Apical–Basal Polarity. Cold Spring Harb Perspect Biol. Cold Spring Harbor Laboratory Press; 2009;1: a000513–a000513. doi:10.1101/cshperspect.a000513

43. Apodaca G, Gallo LI, Bryant DM. Role of membrane traffic in the generation of epithelial cell asymmetry. Nat Cell Biol. 2012;14: 1235–1243. doi:10.1038/ncb2635

44. Bailey TL, Elkan C. Fitting a mixture model by expectation maximization to discover motifs in biopolymers. Proc Int Conf Intell Syst Mol Biol. 1994;2: 28–36.

45. Gupta S, Stamatoyannopoulos JA, Bailey TL, Noble W. Quantifying similarity between motifs. Genome Biology. 2007;8: R24. doi:10.1186/gb-2007-8-2-r24

46. Lyne R, Smith R, Rutherford K, Wakeling M, Varley A, Guillier F, et al. FlyMine: an integrated database for Drosophila and Anopheles genomics. Genome Biology. BioMed Central Ltd; 2007;8: R129. doi:10.1186/gb-2007-8-7-r129

47. Grant CE, Bailey TL, Noble WS. FIMO: scanning for occurrences of a given motif. Bioinformatics. 2011;27: 1017–1018. doi:10.1093/bioinformatics/btr064

48. Huang W, Loganantharaj R, Schroeder B, Fargo D, Li L. PAVIS: a tool for Peak Annotation and Visualization. Bioinformatics. Oxford University Press; 2013;29: 3097–3099. doi:10.1093/bioinformatics/btt520

49. Li R, Gundersen GG. Beyond polymer polarity: how the cytoskeleton builds a polarized cell. Nat Rev Mol Cell Biol. Nature Publishing Group; 2008;9: 860–873. doi:10.1038/nrm2522

50. Schreiber KH, Kennedy BK. When Lamins Go Bad: Nuclear Structure and Disease. Cell. 2013;152: 1365–1375. doi:10.1016/j.cell.2013.02.015

51. Dechat T, Adam SA, Taimen P, Shimi T, Goldman RD. Nuclear Lamins. Cold Spring Harb Perspect Biol. 2010;2: a000547–a000547. doi:10.1101/cshperspect.a000547

52. Chang W, Worman HJ, Gundersen GG. Accessorizing and anchoring the LINC complex for multifunctionality. J Cell Biol. Rockefeller University Press; 2015;208: 11–22. doi:10.1083/jcb.201409047

53. Turkel N, Sahota VK, Bolden JE, Goulding KR, Doggett K, Willoughby LF, et al. The BTB-zinc finger transcription factor abrupt acts as an epithelial oncogene in Drosophila melanogaster through maintaining a progenitor-like cell state. PLoS Genet. 2013;9: e1003627. doi:10.1371/journal.pgen.1003627

54. Sun G, Irvine KD. Regulation of Hippo signaling by Jun kinase signaling during compensatory cell proliferation and regeneration, and in neoplastic tumors. Dev Biol. 2011;350: 139–151. doi:10.1016/j.ydbio.2010.11.036

55. Richardson ECN, Pichaud F. Crumbs is required to achieve proper organ size control during Drosophila head development. Development. 2010;137: 641–650. doi:10.1242/dev.041913

56. Takino K, Ohsawa S, Igaki T. Loss of Rab5 drives non-autonomous cell proliferation through TNF and Ras signaling in Drosophila. Dev Biol. 2014;395: 19–28.

57. Pellinen T, Arjonen A, Vuoriluoto K, Kallio K, Fransen JAM, Ivaska J. Small GTPase Rab21 regulates cell adhesion and controls endosomal traffic of beta1-integrins. J Cell Biol. Rockefeller Univ Press; 2006;173: 767–780. doi:10.1083/jcb.200509019

58. Guelen L, Pagie L, Brasset E, Meuleman W, Faza MB, Talhout W, et al. Domain organization of human chromosomes revealed by mapping of nuclear lamina interactions. Nature. 2008;453: 948–951. doi:10.1038/nature06947

59. Denais C, Lammerding J. Nuclear mechanics in cancer. Adv Exp Med Biol. 2014;773: 435–470. doi:10.1007/978-1-4899-8032-8_20

60. Jaalouk DE, Lammerding J. Mechanotransduction gone awry. Nat Rev Mol Cell Biol. Nature Publishing Group; 2009;10: 63–73. doi:doi:10.1038/nrm2597

61. Schäfer M, Werner S. Cancer as an overhealing wound: an old hypothesis revisited. Nat Rev Mol Cell Biol. Nature Publishing Group; 2008;9: 628–638. doi:10.1038/nrm2455

62. Hsu JC, Laz T, Mohn KL, Taub R. Identification of Lrf-1, a Leucine-Zipper Protein That Is Rapidly and Highly Induced in Regenerating Liver. National Acad Sciences; 1991;88: 3511–3515. doi:10.1073/pnas.88.9.3511

63. Pagliarini RA, Xu T. A genetic screen in Drosophila for metastatic behavior. Science. 2003;302: 1227–1231. doi:10.1126/science.1088474

64. Sotillos S, Díaz-Meco MT, Caminero E, Moscat J, Campuzano S. DaPKC-dependent phosphorylation of Crumbs is required for epithelial cell polarity in Drosophila. J Cell Biol. Rockefeller Univ Press; 2004;166: 549–557. doi:10.1083/jcb.200311031

65. Schulze SR, Curio-Penny B, Li YH, Imani RA, Rydberg L, Geyer PK, et al. Molecular genetic analysis of the nested Drosophila melanogaster lamin C gene. Genetics. 2005;171: 185–196. doi:10.1534/genetics.105.043208

66. Groth AC, Fish M, Nusse R, Calos MP. Construction of Transgenic Drosophila by Using the Site-

Specific Integrase From Phage ϕC31. Genetics. 2004;166: 1775–1782.

67. Livak KJ, Schmittgen TD. Analysis of relative gene expression data using real-time quantitative PCR and the 2(-Delta Delta C(T)) Method. Methods. 2001;25: 402–408. doi:10.1006/meth.2001.1262

68. Lee T, Luo L. Mosaic analysis with a repressible cell marker (MARCM) for Drosophila neural development. Trends Neurosci. 2001;24: 251–254.

69. Sandmann T, Jakobsen JS, Furlong EEM. ChIP-on-chip protocol for genome-wide analysis of transcription factor binding in Drosophila melanogaster embryos. Nat Protoc. Nature Publishing Group; 2006;1: 2839–2855. doi:10.1038/nprot.2006.383

70. Quinlan AR, Hall IM. BEDTools: a flexible suite of utilities for comparing genomic features. Bioinformatics. Oxford University Press; 2010;26: 841–842. doi:10.1093/bioinformatics/btq033

71. Oktaba K, Gutiérrez L, Gagneur J, Girardot C, Sengupta AK, Furlong EEM, et al. Dynamic regulation by polycomb group protein complexes controls pattern formation and the cell cycle in Drosophila. Developmental Cell. 2008;15: 877–889. doi:10.1016/j.devcel.2008.10.005

72. Mundorf J, Uhlirova M. The Drosophila Imaginal Disc Tumor Model: Visualization and Quantification of Gene Expression and Tumor Invasiveness Using Genetic Mosaics. JoVE. 2016;: e54585. doi:10.3791/54585

73. Wagle P, Nikolić M, Frommolt P. QuickNGS elevates Next-Generation Sequencing data analysis to a new level of automation. BMC Genomics. BioMed Central; 2015;16: 487. doi:10.1186/s12864-015-1695-x

74. Li H, Handsaker B, Wysoker A, Fennell T, Ruan J, Homer N, et al. The Sequence Alignment/Map format and SAMtools. Bioinformatics. 2009;25: 2078–2079. doi:10.1093/bioinformatics/btp352

75. Trapnell C, Pachter L, Salzberg SL. TopHat: discovering splice junctions with RNA-Seq. Bioinformatics. 2009;25: 1105–1111. doi:10.1093/bioinformatics/btp120

76. Trapnell C, Williams BA, Pertea G, Mortazavi A, Kwan G, van Baren MJ, et al. Transcript assembly and quantification by RNA-Seq reveals unannotated transcripts and isoform switching during cell differentiation. Nat Biotechnol. 2010;28: 511–515. doi:10.1038/nbt.1621

77. Anders S, Huber W. Differential expression analysis for sequence count data. Genome Biology. BioMed Central; 2010;11: R106. doi:10.1186/gb-2010-11-10-r106

78. Durinck S, Moreau Y, Kasprzyk A, Davis S, De Moor B, Brazma A, et al. BioMart and Bioconductor: a powerful link between biological databases and microarray data analysis. Bioinformatics. 2005;21: 3439–3440. doi:10.1093/bioinformatics/bti525

79. Housden BE, Millen K, Bray SJ. Drosophila Reporter Vectors Compatible with ΦC31 Integrase Transgenesis Techniques and Their Use to Generate New Notch Reporter Fly Lines. G3: Genes|Genomes|Genetics. Genetics Society of America; 2012;2: 79–82. doi:10.1534/g3.111.001321

80. Faul F, Erdfelder E, Buchner A, Lang A-G. Statistical power analyses using G*Power 3.1: tests for correlation and regression analyses. Behav Res Methods. 2009;41: 1149–1160. doi:10.3758/BRM.41.4.1149

Author contribution

C.D., A.C., G.C. and M.U. conceived the study, designed and performed the experiments, and analyzed the data. M.J. prepared the SEM samples. B.H and C.Kl. developed and described the CoPrA workflow. C.D., C.Kl., and B.H. analyzed the ChIP-seq data. C.D., G.C., M.U., and M.J. wrote the paper. M.U. acquired funding.

Figure legends

Fig 1. *atf3* is a polarity response gene

(A) Transcript levels of *atf3* increased in *scrib*^{1} mutant larvae and in adult heads bearing *dlg1*^{G0342} clones relative to control. qRT-PCR data are means of 5 and 3 biological replicates (*FRT82B* and *FRT82B scrib*^{1}, respectively) and 5 and 4 biological replicates (*FRT19* and *FRT19 dlg1*^{G0342}, respectively). Error bars depict 95% confidence interval; Unpaired Student's t-tests assuming unequal variance were used to calculate p-values: *p=0.014, **p=0.0051. **(B-C)** Atf3::GFP fusion protein expressed from a recombineered BAC (*atf3*^{gBAC}) labeled differentiated photoreceptors and a subset of peripodial cells in the control eye/antennal imaginal disc (B). In wing imaginal disc, peripodial cells (C) and columnar cells forming a ring surrounding the wing pouch (C', arrows) showed Atf3::GFP enrichment. (**D-E**) Increase of Atf3:GFP signal appeared in the posterior compartment of the wing imaginal disc where Dlg1 (D-D') or Scrib (E-E') was depleted. **(F-I)** Clones in the EAD (myr-mRFP) deficient for Dlg1 expressed ectopic Atf3 within the eye (F') and antenna (G') part, which persisted when JNK signaling was blocked (*dlg1*^{G0342} *bsk*^{DN}) (H', I'). (**J**) Mild activation of JNK in the posterior compartment (J) of the wing imaginal disc (*en>hep*^{wt}) induced TRE-DsRed (J') but did not trigger expression of GFP-tagged Atf3 (J''). (**K,L**) Atf3 protein levels increased following expression of a membrane tethered aPKC in the posterior compartment of the wing imaginal disc (*en>aPKC*^{CAAX}) (K'). This induction was independent of JNK signaling (*en>aPKC*^{CAAX} *bsk*^{DN}) (L'). (**M-P**) Driving Atf3 (M) or aPKC^{CAAX} (O) with *dpp-GAL4* (mCherry) induces an Atf3-responsive ATRE-GFP reporter (M',O'), which is insensitive to Hep (N') or activated Yki (P'). The wing discs (C-D, M-P) or the posterior wing disc compartments (E,J) are outlined with dotted lines. Micrographs B and F-I are projections of multiple confocal sections, while micrographs C-E and J-P are single slices. To allow for comparisons, micrographs M-P were acquired

with the same microscope settings. Scale bars: 50 μm (B-I,K-L) and 100 μm (J,M-P).

Fig 2. *atf3* genetically interacts with *dlg1*

(A-R) *eyFLP*-mediated mitotic recombination was used to generate clones (GFP) in EADs of the indicated genotypes. Lack of *dlg1* (C) produced smaller adult eyes containing patches of undifferentiated tissue (C′) relative to control eyes (A,A′) and those bearing $atf3^{76}$ mutant clones (B,B′). Simultaneous clonal loss of *atf3* and *dlg1* (D) resulted in normally sized eyes with few to no differentiation defects (D′). In contrast, overexpression of *atf3* in $dlg1^{G0342}$ clones (E) exacerbated the differentiation defects (E′). Clonal overexpression of *atf3* alone disturbed the orderly ommatidia array (F) generating glossy patches lacking bristles (F′). The $dlg1^{G0342}$ (I) and $atf3^{76}dlg1^{G0342}$ (J) EAD clones were less abundant and smaller relative to control (G) and $atf3^{76}$ mutant clones (H). Overexpression of *atf3* in $dlg1^{G0342}$ cells generated clones with smooth boundaries composed of large, round cells (K). Overexpression of *atf3* alone did not impact clone shape or abundance (L). While no extrusion was observed either in case of $atf3^{76}$ mutant (N) or *atf3* overexpressing (R) EAD clones compared to control EADs (M), the clonal loss of *dlg1* induced both apical and basal extrusion (O). Clones that lack *dlg1* and overexpress *atf3* are extruded apically (Q), while simultaneous loss of *dlg1* and *atf3* normalizes the epithelial integrity (P). EADs M-R were stained against the p120-catenin to aid the assessment of tissue architecture. Discs were counterstained with DAPI. Micrographs A-F are scanning electron micrographs. Micrographs G-R are projections of multiple confocal sections and show EADs 7 days after egg laying. Dotted lines indicate cross sections, which appear below the corresponding panels and are oriented apical side up. Scale bars: 100 μm (A-F), 10 μm (A′-F′), 100 μm (G-L), 50 μm (M-R).

Fig 3. Loss of *atf3* restores differentiation and polarity to *dlg1* mutant clones

(A-F) *eyFLP*-mediated mitotic recombination was used to generate clones (GFP) in the EADs of the indicated genotypes. (**A-C**) Immunostaining shows the stereotypical pattern of differentiated photoreceptors (Elav) and the lateral membrane component Fasciclin III (FasIII) in control discs (A′-A′′). Patterns of these markers are disturbed in $dlg1^{G0342}$ clones (B′- B′′), and restored in $atf3^{76}dlg1^{G0342}$ clones (C′- C′′). Similar to control (A′′), $atf3^{76}dlg1^{G0342}$ cells (C′′) show columnar organization and maintain contact with the apical surface while $dlg1^{G0342}$ clones delaminate (B′′). (**D-E**) The normal patterns of the adherens junction component DE-cadherin (DE-cad) (D′) and the apical determinant Crumbs (D′′) are disturbed in $dlg1^{G0342}$ clones (E′-E′′) but normalized in $atf3^{76}dlg1^{G0342}$ clones (F′-F′′). Discs were counterstained with DAPI. White arrows indicate cross sections, which appear below the corresponding panels and are oriented apical side up. Clones are outlined with white dotted lines. Micrographs are otherwise single confocal slices. All images show EADs 7 days after egg laying. Scale bars: 20 μm (A-F).

Fig 4. Impairment of Rab5 and Rab11 abundance and localization in *dlg1* mutant clones is Atf3-dependent

(**A-D**) *eyFLP*-mediated mitotic recombination combined with a co-expression of p35 was used to generate larger clones (GFP) in the EADs of the indicated genotypes. (**A-D**) The levels and localization of early Rab5-positive endosomes are disturbed upon loss of *dlg1* both posterior (A′) and anterior (B′) to the morphogenetic furrow, while recycling Rab11 vesicles are enriched in *dlg1* mutant clones relative to surrounding tissue (A′′,B′′). Both Rab5 and Rab11 vesicle amounts and distribution are normalized in $atf3^{76}dlg1^{G0342}$ double mutant clones (C-D). On the cross sections, blue arrowheads

indicate the regular Rab5 enrichment along the photoreceptors (A′,C′), yellow arrowheads indicate the apical localization of Rab5 in epithelial cells anterior of the MF (B′,D′). Note that both patterns are lost in *dlg1* deficient cells. Discs were counterstained with DAPI. White arrows indicate cross sections, which appear below the corresponding panels and are oriented apical side up. Clones are outlined by white dotted lines. All images show EAD 7 days after egg laying. Scale bars: 10 μm (A,C), 20 μm (B,D).

Fig 5. Atf3 targets genes fundamental to epithelial cytoarchitecture

(**A**) ChIP-seq identified 152 genomic positions bound by Atf3 in samples from $atf3^{76}/Y;;atf3^{8BAC}/+$ adult flies. (**B**) 112 genomic regions, proximal to 121 genes, contained the *Drosophila* Atf3 motif. The core of the Atf3 motif closely matches the CRE element but not the AP-1 consensus site. The Atf3 motif most closely resembles the *Drosophila* Atf2 motif (*p=5E-7*) and human JDP2/ATF3 motif (*p=3E-9*). (**C**) Of the 121 genes targeted by Atf3, 40 have roles in cytoskeleton dynamics. (**D)** A schematic shows Atf3 targets (orange) belonging to the cytoskeleton GO cluster broken into subgroups and placed within representative spatial contexts in an epithelial cell. **(E)** Transcriptome analysis identified a total of 4957 genes that were differentially regulated by a factor ≥1.5 in mosaic EADs expressing Atf3 ($eyFLP^{MARCM}$ $atf3^{wt}$). Three times as many genes were transcriptionally repressed (n=3666) than activated (n=1291). **(F)** A table lists the Flybase ID, gene symbol (Symbol), and relative fold change in gene expression (Fold Change *FRT82B* $atf3^{wt}$/*FRT82B*) of the 32 Atf3 targets identified by ChIP-seq which were differentially regulated in mosaic EADs expressing Atf3. Symbols for genes belonging to the cytoskeleton-related GO clusters are underlined. **(G)** A list summarizing the regulation of all tubulin genes in mosaic EADs overexpressing Atf3 ($eyFLP^{MARCM}$ $atf3^{wt}$) sorted in descending order of transcript abundance.

Fig 6. LamC is a *bona fide* target of Atf3

(**A-B**) Both Atf3 overexpression (*en>atf3*^{wt}) and Scrib knockdown (*en>scrib*^{RNAi}) increased LamC levels in the posterior compartment of the wing imaginal disc (mCherry) (A′,B′). (**C-D**) *eyFLP*-mediated clonal overexpression of Atf3 (GFP) markedly upregulated the LamC protein (D′) compared to levels detected in surrounding tissue and control clones (C′). (**E-F**) LamC was also enriched in *dlg1*^{G0342} clones (E′), but was reduced below control levels in *atf3*^{76}*dlg1*^{G0342} cells (F′). Discs were counterstained with DAPI. Images represent single slices from confocal stacks. The wing disc posterior compartments (A-B) and EAD clones (C-F) are outlined with white dotted lines. On images C′-F′, the arrows indicate cross sections shown below the corresponding images, with the apical side facing up. Scale bars: 50 μm (A-B), 10 μm (C-F).

Fig 7. Increased Atf3 levels disturb the microtubule network

(**A-B)** Columnar cells in the wing disc expressing Atf3 (*hsFLPout>>atf3*^{wt}) (GFP) contained less apical, subcortical α- and β-Tubulin compared to surrounding tissue (A′,B′) and non-clonal cells of the peripodial epithelium (P) directly above (A′). **(C)** Wing disc clones expressing Atf3 display lower levels of non-centrosomal γ-Tubulin (C′). **(D-F)** *eyFLP*-mediated mitotic recombination was used to generate clones (GFP) in the EADs of the indicated genotypes. Clones lacking *dlg1* (E) show disturbed α-Tubulin localization (E′) compared to control clones (D-D′) in the photoreceptor region of the EADs. Clones lacking both *dlg1* and *atf3* (F) show normalized microtubule distribution along the apicobasal axis (F′). Discs were counterstained with DAPI. The arrows indicate cross sections shown below the corresponding images, with the apical side facing up. Clones are outlined with white dotted lines. Scale bars: 10 μm (A-F).

Fig 8. Model depicting the effects of Atf3 misregulation in epithelia

In our working model (upper diagram), loss of *dlg1* activates aPKC and JNK signaling. Through Fos, JNK induces apoptosis and restrains excessive cell proliferation that would result from aPKC-mediated activation of Yki. Dlg1 mutant cells flatten and are extruded. Aberrant aPKC activity induces Atf3 expression independent of Yki and JNK, leading to defects in cell morphology and differentiation. Columnar cell organization and the aberrant distribution of Rab5 and Rab11 vesicles and polarity proteins observed upon loss of Dlg1 are rescued by simultaneous loss of Atf3, while JNK signaling remains active. Atf3 overexpression negatively impacts the microtubule network, dysregulates Rab5 and Rab11 trafficking routes, and perturbs the distribution of apicobasal polarity proteins. Nevertheless, Atf3 overexpressing cells remain columnar. Note that in all cases, LamC is regulated in an Atf3-dependent manner. Physiological levels/correct localization are indicated in blue, increased levels/expanded localization in green and reduced levels/mislocalization in red.

Supplementary material

S1 Fig. The *dlg1*^{G0342} mutation is a loss-of-function allele

(A) No *dlg1* transcript is detected in hemizygous *dlg1*^{G0342} larvae relative to control. **(B-E)** *eyFLP*-mediated mitotic recombination was used to generate clones (GFP) in the EADs of the indicated genotypes. Homozygous *dlg1*^{G0342} and *atf3*^{76} *dlg1*^{G0342} EAD clones (B-C and D-E, respectively) are deficient for Dlg1 protein (C′,E′). qRT-PCR data are means of 6 biological replicates. Error bars depict 95% confidence interval; Unpaired Student's t-tests assuming unequal variance were used to calculate p-values: ***= $p<0.001$. Scale bars: 100 μm (B,D), 10 μm (C,E).

S2 Fig. Atf3 activates an ATRE reporter in cell culture

(A,B) In S2 cells, Atf3 induced the ATRE-RFP reporter compared to undetectable activity in control cells. **(C,D)** Atf3 did not activate a mutant mATRE-RFP reporter. **(E-G)** Expression of FLAG::Atf3 strongly induced an ATRE-GFP reporter in S2 cells. While co-expression of Hep/JNKK and Bsk/JNK induced an AP-1 reporter (TRE-DsRed) (G) it only weakly activated the ATRE reporter (E). α-Spectrin served as a loading control.

S3 Fig. Atf3 drives specific phenotypes in *dlg1* null mutant mosaic eyes

(A-G) *eyFLP*-mediated mitotic recombination was used to generate clones of the indicated genotypes in the eye. Homozygous $dlg1^{G0342}$ or $dlg1^{m52}$ EAD clones lead to smaller adult eyes of irregular shape (F,G) containing patches of undifferentiated tissue (A,D) relative to control (Fig 2A). Adult eyes derived from $atf3^{76}$ $dlg1^{G0342}$ or $atf3^{76}$ $dlg1^{m52}$ mosaic EADs exhibit mild or no differentiation defects (B,E) as well as restored eye size and shape (F,G). A single copy of a genomic $atf3^{gBAC}$ reinstates differentiation defects to $atf3^{76}$ $dlg1^{G0342}$ adult eyes (C). Outlines of adult eyes from the indicated genotypes are presented vertically aligned along their midline (G). Adult eye measurements were performed from at least 17 biological replicates. Error bars depict 95% confidence interval; Unpaired Student's t-tests assuming unequal variance were used to calculate p-values: ***= $p<0.001$ ****$p<0.0001$.

S4 Fig. Clonal expression of *atf3* does not impact differentiation in the EAD

(A-D) *eyFLP*-mediated mitotic recombination was used to generate clones (GFP) in the EAD of the indicated genotypes. $dlg1^{G0342}$ mutant cells located to the left of the morphogenetic furrow (arrow) are often Elav-negative (A,B) compared to a regular Elav staining pattern in the $atf3^{wt}$ clones (C,D) and the

non-clonal neighbors. Discs were counterstained with DAPI. Micrographs are single confocal slices. All images show EADs 7 days after egg laying. Scale bars: 100 μm (A,C), 20 μm (B,D).

S5 Fig. JNK signaling is elevated upon loss of polarity and blocking apoptosis does not mitigate the genetic interaction between Atf3 and Dlg1

(A-H) *eyFLP*-mediated mitotic recombination was used to generate GFP-labeled clones of the indicated genotypes in the EAD. **(A)** Flow cytometry determined the number of GFP+ cells in EADs bearing clones of the indicated genotypes. Relative to control (n=4), $dlg1^{G0342}$ (n=3) , $atf3^{76}$ $dlg1^{G0342}$ (n=4), and $dlg1^{G0342}$ $atf3^{wt}$ (n=5) clones were less abundant. $dlg1^{G0342}$ $atf3^{wt}$ cells were less frequent relative to $dlg1^{G0342}$ alone. Blocking apoptosis raised the relative abundance of $dlg1^{G0342}$ (n=7) and $atf3^{76}$ $dlg1^{G0342}$ (n=6) cells, but not to control (n=4) levels. Unpaired Student's t-tests assuming unequal variance were used to calculate p-values. Error bars reflect the 95% confidence interval. ***= $p<0.001$. **(B-C)** An AP-1 reporter (TRE-DsRed) serves as a readout of JNK pathway activity and is upregulated in $dlg1^{G0342}$ (B') and $atf3^{76}dlg1^{G0342}$ (C') EAD clones. **(D)** The eclosion rate of animals bearing $atf3^{76}dlg1^{G0342}p35$ EAD was less than control but was four times higher than animals bearing $dlg1^{G0342}p35$ EAD. Four biological replicates were used for each genotype. Unpaired Student's t-tests assuming unequal variance were used to calculate p-values: ***= $p<0.001$. **(E-H)** Compared to control (E), adult eyes derived from $dlg1^{G0342}p35$ EAD were very small, comprising mostly undifferentiated tissue (F), while those derived from $atf3^{76}dlg1^{G0342}p35$ EAD exhibited only traces (G) or small patches (H) of defective photoreceptor differentiation. (**I-K**) The EGUF/hid technique was used to generate adult eyes comprised entirely of control (I), $dlg1^{G0342}$ (J) and $atf3^{76}dlg1^{G0342}$ (K) clonal tissue as non-clonal cells were removed by expression of pro-apoptotic protein Hid. Compared to control (I), $dlg1^{G0342}$ eyes were severely reduced in size with only traces of ommatidia left (J). $atf3^{76}dlg1^{G0342}$ eyes were only mildly reduced relative to

control and contained several rows of orderly arranged ommatidia (K). Micrographs (B,C) are projections of multiple confocal sections showing EADs 7 days after egg laying. Scale bars: 100 μm (B,C).

S6 Fig. Epithelial clones lacking *dlg1* show Atf3-dependent perturbation of early endosomes, but no defects in endocytosis

(**A-F**) *eyFLP*-mediated mitotic recombination was used to generate clones (GFP) in the EADs of the indicated genotypes. Apoptosis of mutant cells was reduced by p35 overexpression. (**A-C**) dlg^{G03421} and $atf3^{76}dlg1^{G0342}$ clones show no disturbances in the uptake of fluorescently labeled dextran (B′- C′) compared to control clones (A′). (**D-E**) The regular pattern of the early endosomal marker Avl (D′) is disrupted in *dlg1* mutant cells (E′), but restored in $atf3^{76}dlg1^{G0342}$ double mutant clones (F′). Discs were counterstained with DAPI. White arrows indicate cross sections, which appear below the corresponding panels and are oriented apical side up. Clones are outlined by white dotted lines. All images show EAD 7 days after egg laying. Scale bars: 10 μm (A-F).

S7 Fig. Removal of *atf3* restores distribution of Rab5-positive vesicles in *dlg1* mutant clones

(A-F) *eyFLP*-mediated mitotic recombination was used to generate clones (GFP) in the EADs of the indicated genotypes. Lower levels and disturbed pattern of the early endosome marker Rab5 (B′,E′) observed in $dlg1^{G0342}$ clones relative to surrounding and control tissue (A′,D′) were largely restored in $atf3^{76}dlg1^{G0342}$ clones (C′,F′). Discs were counterstained with DAPI. In A-C, EADs and in D′-F′, clones are outlined with dotted white lines. White arrows indicate cross sections, which appear below the corresponding panels and are oriented apical side up. On the cross sections of D′-F′, arrowheads indicate the regular Rab5 accumulation in the photoreceptors. Micrographs are projections of multiple

confocal slices (A-F). Scale bars: 100 μm (A-C), 20 μm (D-F).

S8 Fig. Gain of Atf3 alters cellular trafficking machinery and the localization of polarity determinants

(A-B) Abundance of Rab5 vesicles (A′) was reduced in cells expressing Atf3 (*hsFLPout>>atf3*^{wt}) (GFP), compared to surrounding tissue while the amount of Rab11 endosomes increased and showed a distinct basal accumulation in Atf3 overexpressing cells (*en>atf3*^{wt}) (GFP) compared to wild type epithelium (B′). (**C-D**) Cross sections of immunostained wing imaginal disc clones expressing Atf3 (*hsFLPout>>atf3*^{wt}) revealed lower levels of the polarity determinant Crumbs on the apical surface (C′). In contrast, the βPS integrin Myospheroid (Mys) appeared to be more abundant in Atf3 overexpressing cells and was distributed along the lateral membranes (D′). White dotted lines indicate clones (A,C,D) or the posterior compartment (B) in the wing disc. Arrowheads indicate cross sections, which appear below the corresponding panels and are oriented apical side up. Micrographs are otherwise single confocal slices. Scale bars: 10 μm (A-D).

S9 fig. Atf3 binds to ATRE sites in the LamC gene and induces LamC transcription in larval EADs

(**A**) Independent qRT-PCR from newly isolated mosaic EADs confirmed RNA-seq results showing enrichment of *LamC*, *dynactin*, *ude* and *arp1* transcripts in EADs overexpressing Atf3 (n=3) relative to control (n=3) while *alphaTub84B* and *betaTub56D* remained unchanged. (**B**) ChIP from third instar EADs followed by qPCR was used to quantify enrichment of the indicated Atf3 sites in *atf3*^{gBAC} samples (n=3) relative to *w*^{1118} control (n=3). *LamC* and *α-Tub84B* were enriched in *atf3*^{gBAC} samples compared to control. Note that *LamC* was bound by Atf3 at two of the three Atf3 sites within the gene.

Atf3 did not bind the ATRE site in *coracle* which was occupied in samples from adults. Error bars indicate 95% confidence interval; Unpaired Student's t-tests assuming unequal variance were used to calculate p-values: **p=0.007 (*LamC*), *p=0.018 (*dynactin*), **p=0.008 (*ude*), **p=0.024 (*arp1*).

S10 Fig. Transcriptional response to gain of Atf3 overlaps with genes misregulated by depletion of the Scrib polarity module

(A-B) Venn diagrams show the overlap between genes differentially regulated by a factor ≥1.5 in mosaic EADs overexpressing Atf3 ($eyFLP^{MARCM}$ $atf3^{wt}$) and wing imaginal discs of $scrib^{1}$ homozygous or $dlg^{40\text{-}2}/Y$ hemizygous mutant larvae. Contingency tables provide information about directionality of expression of shared transcripts between the two datasets and serve to calculate the significance of overlap using a one-tailed Fisher Exact Probability test.

S11 Fig. LamC overexpression in imaginal disc cells is not sufficient to recapitulate Atf3 gain-of-function phenotypes

(A-B) Immunostaining for α-Tubulin (A) and Crumbs (B) is unchanged in wing imaginal disc clones (GFP) expressing wild type LamC (*hsFLPout>>LamC*). Discs were counterstained with DAPI. Clones are outlined with dotted white lines. White arrows indicate cross sections, which appear below the corresponding panels and are oriented apical side up. Scale bars: 10 μm (A,B).

S1 Table. Summary of oligonucleotides

S2 Table. Summary of fly crosses

S1 Dataset. Atf3 ChIP-seq peaks and targets

(A) Dataset All Peaks (n=152). The chromosomal positions (Chromosome, Peak Start, Peak End) of the 152 regions differentially enriched in Atf3 ChIP samples are given .

(B) Dataset Atf3 Peaks (n=112). Results from MEME (Bailey and Elkan, 1994), identifying a consensus Drosophila Atf3 motif in 112 peaks. For each peak containing the *Drosophila* Atf3 motif, the Start Position and End Position are given, and the probability of a random string having the same MEME match score or higher (p-value) is also provided. The core twelve nucleotide sequence (Atf3 Motif Sequence) and the immediate upstream and downstream sequence (5' Flanking Sequence, 3' Flanking Sequence) of each Atf3 motif are given. Genes most proximal to the Atf3 motifs are provided as FlyBase identifiers (Associated Genes (Symbols) and Associated Genes (FlyBase ID)).

(C) Dataset Cytoskeleton GO. Genes belonging to at least one of five cytoskeleton gene ontology (GO) terms (actin binding GO_0003779, calponin homology domain IPR_001715, cytoskeletal protein binding GO_0008092, cytoskeleton organization GO_0007010, cytoskeleton GO_0005856) are listed with their CG Number, Gene Symbol, and FlyBase ID. GO terms are arranged in columns. Genes belonging to a given GO term are indicated with green cells containing an "x".

S2 Dataset. *Drosophila* Atf3 PMW

S3 Dataset. Transcriptomic analysis of mosaic EADs

Figure 1

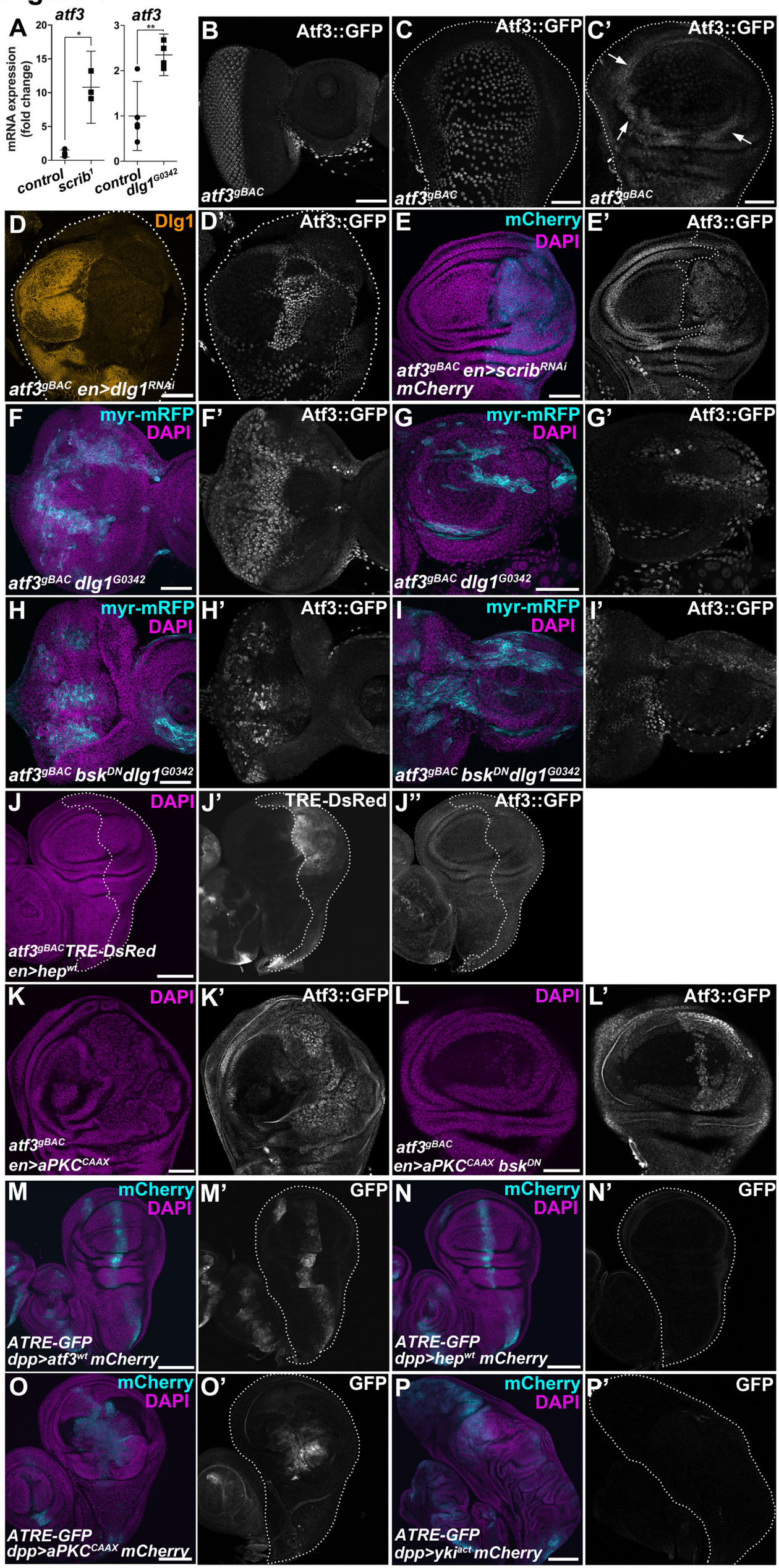
A
atf3
atf3
mRNA expression (fold change)
control
scrib1
control
dlg1G0342
B Atf3::GFP
atf3gBAC
C Atf3::GFP
atf3gBAC
C' Atf3::GFP
atf3gBAC
D Dlg1
atf3gBAC en>dlg1RNAi
D' Atf3::GFP
E mCherry DAPI
atf3gBAC en>scribRNAi mCherry
E' Atf3::GFP
F myr-mRFP DAPI
atf3gBAC dlg1G0342
F' Atf3::GFP
G myr-mRFP DAPI
atf3gBAC dlg1G0342
G' Atf3::GFP
H myr-mRFP DAPI
atf3gBAC bskDN dlg1G0342
H' Atf3::GFP
I myr-mRFP DAPI
atf3gBAC bskDN dlg1G0342
I' Atf3::GFP
J DAPI
atf3gBAC TRE-DsRed en>hepwt
J' TRE-DsRed
J'' Atf3::GFP
K DAPI
atf3gBAC en>aPKCCAAX
K' Atf3::GFP
L DAPI
atf3gBAC en>aPKCCAAX bskDN
L' Atf3::GFP
M mCherry DAPI
ATRE-GFP dpp>atf3wt mCherry
M' GFP
N mCherry DAPI
ATRE-GFP dpp>hepwt mCherry
N' GFP
O mCherry DAPI
ATRE-GFP dpp>aPKCCAAX mCherry
O' GFP
P mCherry DAPI
ATRE-GFP dpp>yki act mCherry
P' GFP

Figure 2

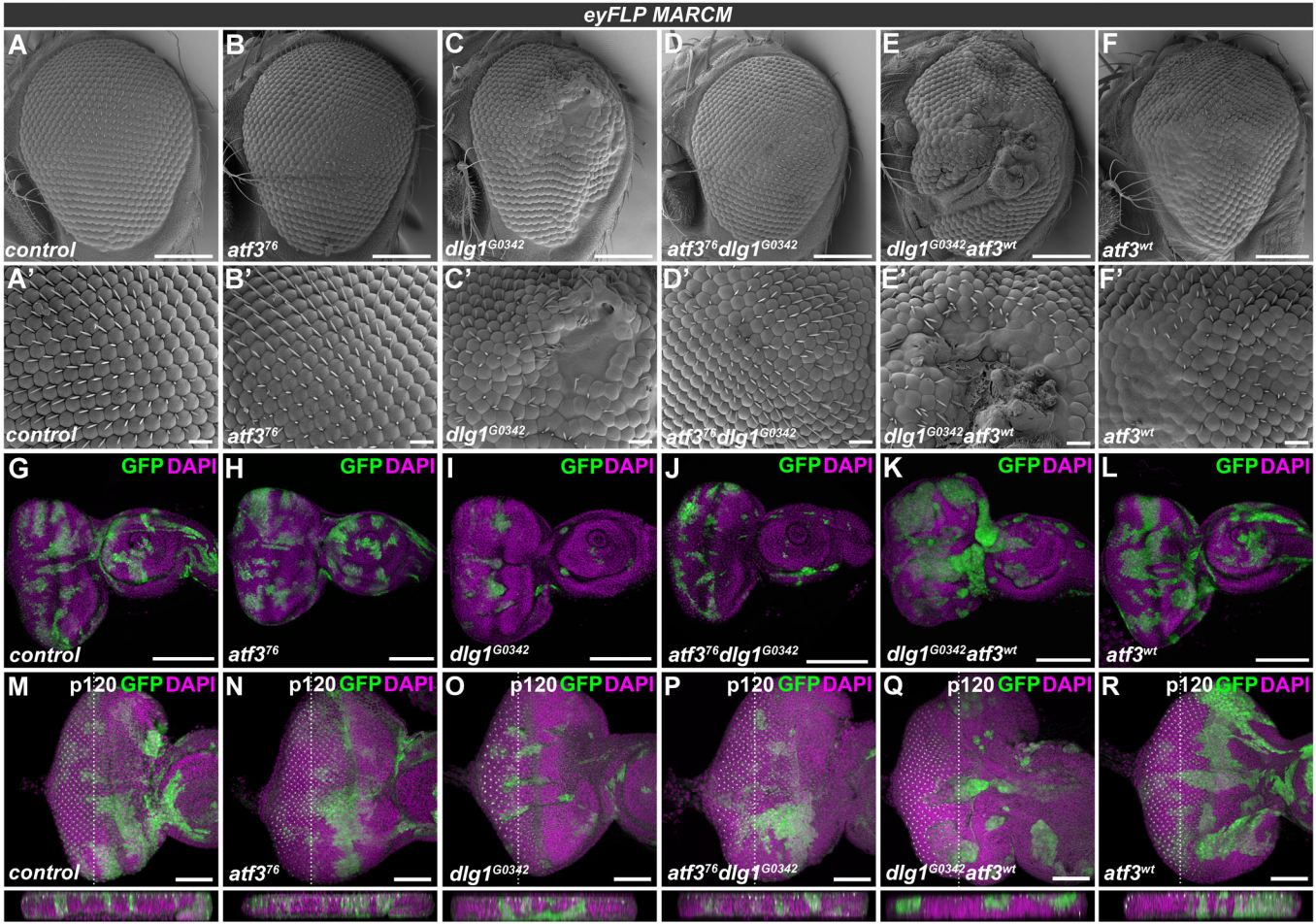
eyFLP MARCM
A
control
B
atf3^76
C
dlg1^G0342
D
atf3^76dlg1^G0342
E
dlg1^G0342atf3^wt
F
atf3^wt
A'
control
B'
atf3^76
C'
dlg1^G0342
D'
atf3^76dlg1^G0342
E'
dlg1^G0342atf3^wt
F'
atf3^wt
G
GFP DAPI
control
H
GFP DAPI
atf3^76
I
GFP DAPI
dlg1^G0342
J
GFP DAPI
atf3^76dlg1^G0342
K
GFP DAPI
dlg1^G0342atf3^wt
L
GFP DAPI
atf3^wt
M
p120 GFP DAPI
control
N
p120 GFP DAPI
atf3^76
O
p120 GFP DAPI
dlg1^G0342
P
p120 GFP DAPI
atf3^76dlg1^G0342
Q
p120 GFP DAPI
dlg1^G0342atf3^wt
R
p120 GFP DAPI
atf3^wt

Figure 3

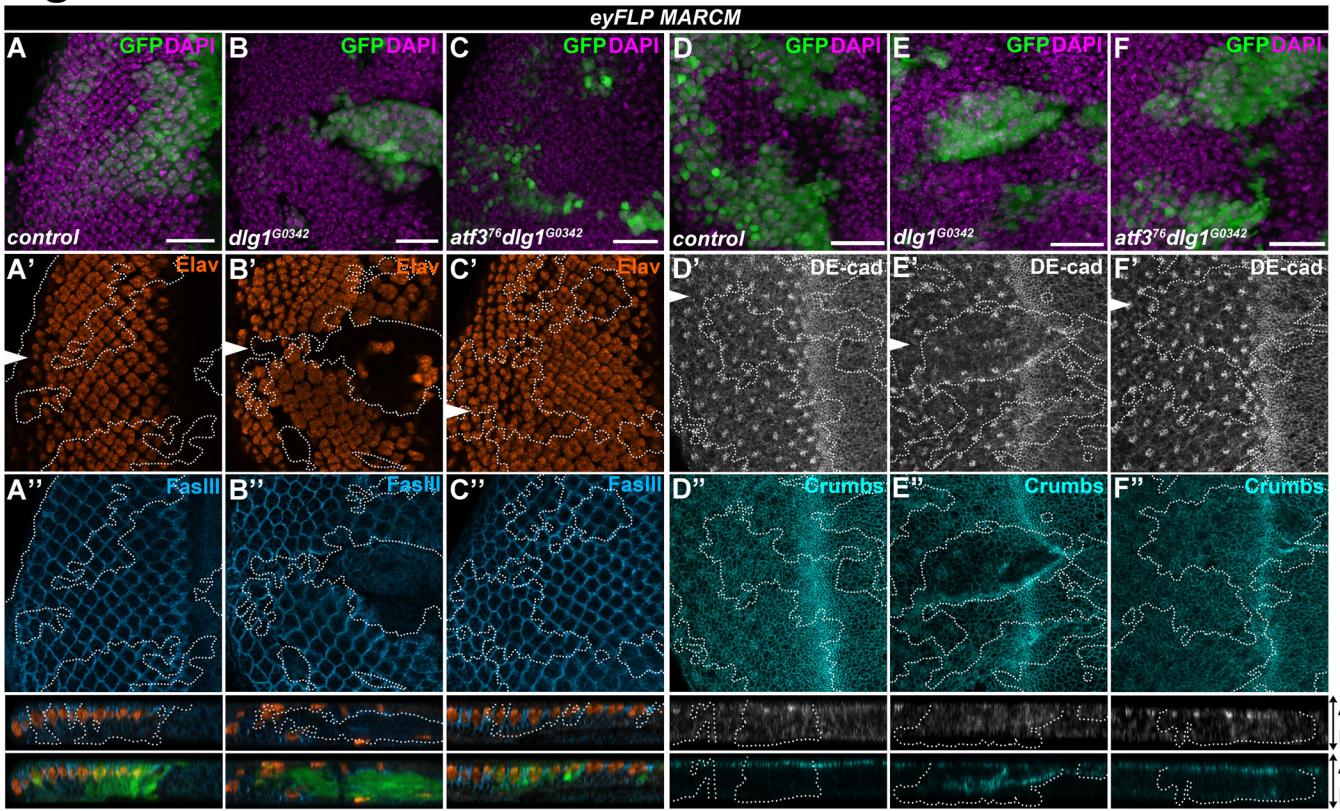
eyFLP MARCM
A
GFP DAPI
control
B
GFP DAPI
dlg1G0342
C
GFP DAPI
atf376dlg1G0342
D
GFP DAPI
control
E
GFP DAPI
dlg1G0342
F
GFP DAPI
atf376dlg1G0342
A'
Elav
B'
Elav
C'
Elav
D'
DE-cad
E'
DE-cad
F'
DE-cad
A''
FasIII
B''
FasIII
C''
FasIII
D''
Crumbs
E''
Crumbs
F''
Crumbs
A
B
A
B

Figure 4

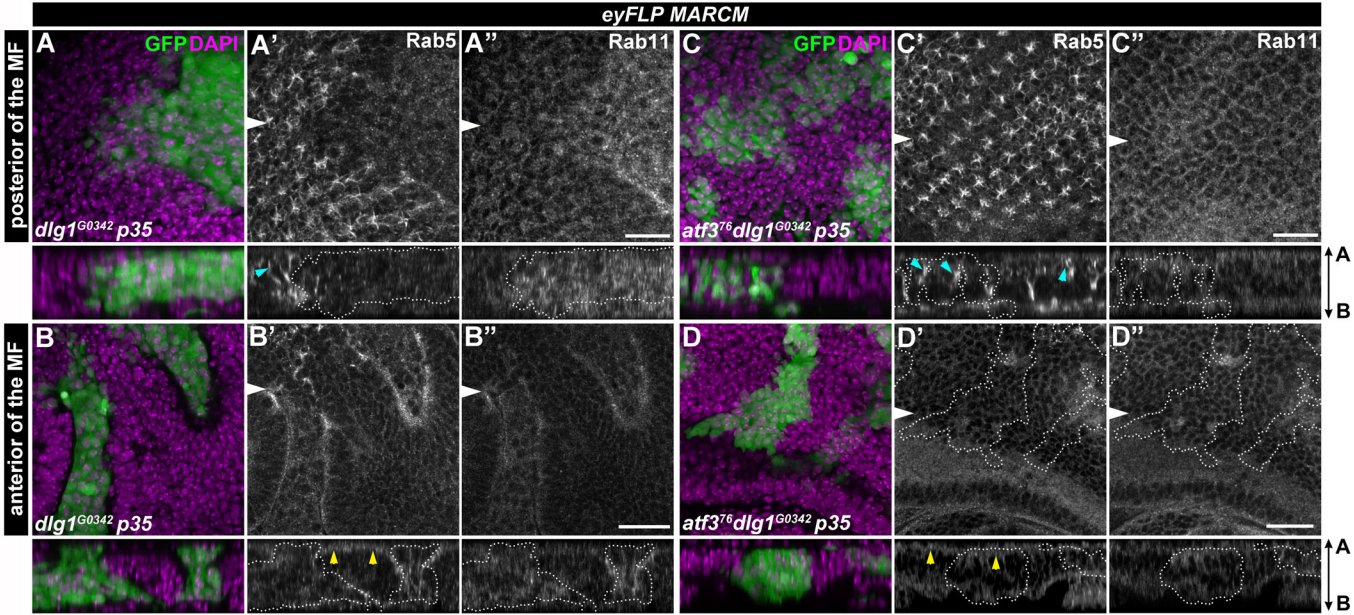
eyFLP MARCM
posterior of the MF
anterior of the MF
A
GFP DAPI
dlg1G0342 p35
A'
Rab5
A''
Rab11
C
GFP DAPI
atf376 dlg1G0342 p35
C'
Rab5
C''
Rab11
B
dlg1G0342 p35
B'
B''
D
atf376 dlg1G0342 p35
D'
D''
A
B
A
B

Figure 5

A

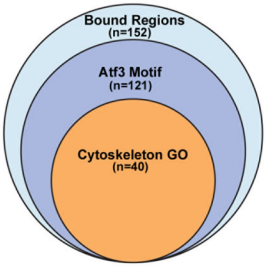

C

GO Term	GO ID	p-Value	# of Genes
actin binding	GO:0003779	1.2E-11	16
cytoskeleton organization	GO:0007010	1.2E-09	29
cytoskeletal protein binding	GO:0008092	4.7E-09	19
calponin homology domain	IPR001715	8.2E-05	7
cytoskeleton	GO:0005856	1.4E-03	20

E

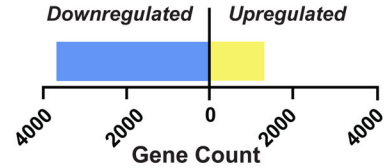

B

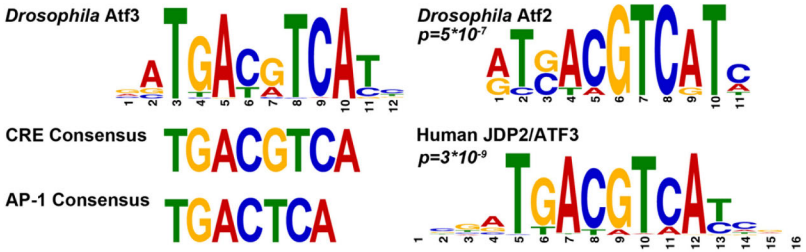

D

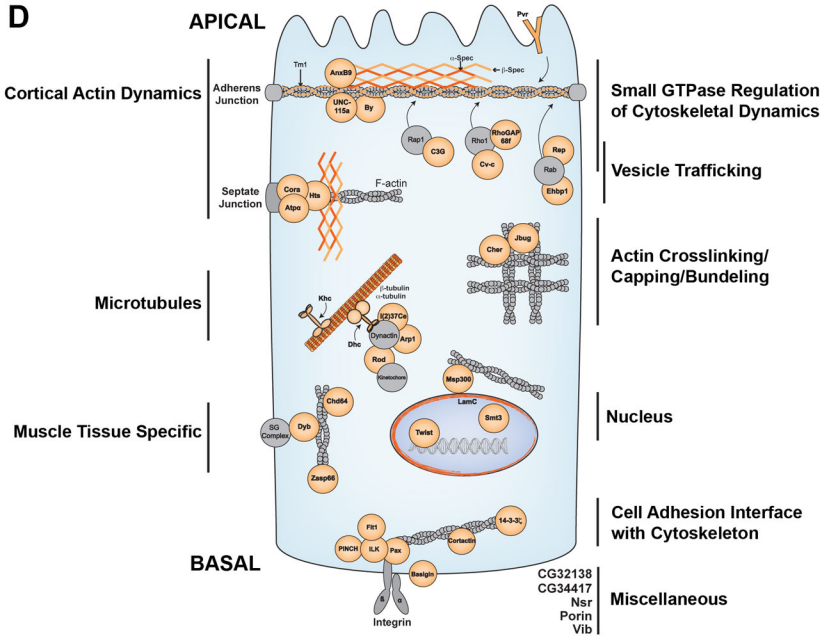

F

Flybase ID	Symbol	Fold change
ChIP targets		FRT82B atf3^{wt}/FRT82B
FBgn0039226	*Ude*	8.28
FBgn0030309	*CG1572*	5.62
FBgn0010397	*LamC*	5.25
FBgn0028543	*NimB2*	4.13
FBgn0034194	*CG15611*	2.52
FBgn0038536	*CG7655*	2.38
FBgn0051347	*CG31347*	2.29
FBgn0032845	*CG10747*	2.11
FBgn0028515	*EndoGI*	2.04
FBgn0033115	*Spn42De*	2.04
FBgn0086446	*DCTN6-p27*	1.96
FBgn0033919	*CG8547*	1.91
FBgn0034755	*CG3746*	1.91
FBgn0028427	*Ilk*	1.9
FBgn0037231	*Vps24*	1.89
FBgn0037465	*CG1105*	1.87
FBgn0035499	*Chd64*	1.84
FBgn0013771	*Cyp6a9*	1.72
FBgn0037518	*CG2641*	1.7
FBgn0011745	*Arp1*	1.63
FBgn0030433	*mRpL49*	1.58
FBgn0026378	*Rep*	1.55
FBgn0026415	*Idgf4*	1.53
FBgn0086708	*stv*	-1.62
FBgn0002932	*neur*	-1.64
FBgn0035113	*pyx*	-1.65
FBgn0000568	*Eip75B*	-1.69
FBgn0262599	*SmydA-3*	-1.7
FBgn0010113	*hdc*	-1.71
FBgn0063923	*Kaz1-ORFB*	-1.79
FBgn0263995	*cpo*	-1.99
FBgn0266100	*CG44837*	-6.02

G

Flybase ID	Symbol	Fold change
Tubulins		FRT82B atf3^{wt}/FRT82B
FBgn0003884	*αTub84B*	n.s.
FBgn0003887	*βTub56D*	1.2
FBgn0003888	*βTub60D*	-1.43
FBgn0003885	*αTub84D*	1.25
FBgn0260639	*γTub23C*	1.13
FBgn0003890	*βTub97EF*	1.29
FBgn0003886	*αTub85E*	n.s.
FBgn0010097	*γTub37C*	-2.53
FBgn0087040	*αTub67C*	-1.37
FBgn0003889	*βTub85D*	-10.47

Figure 6

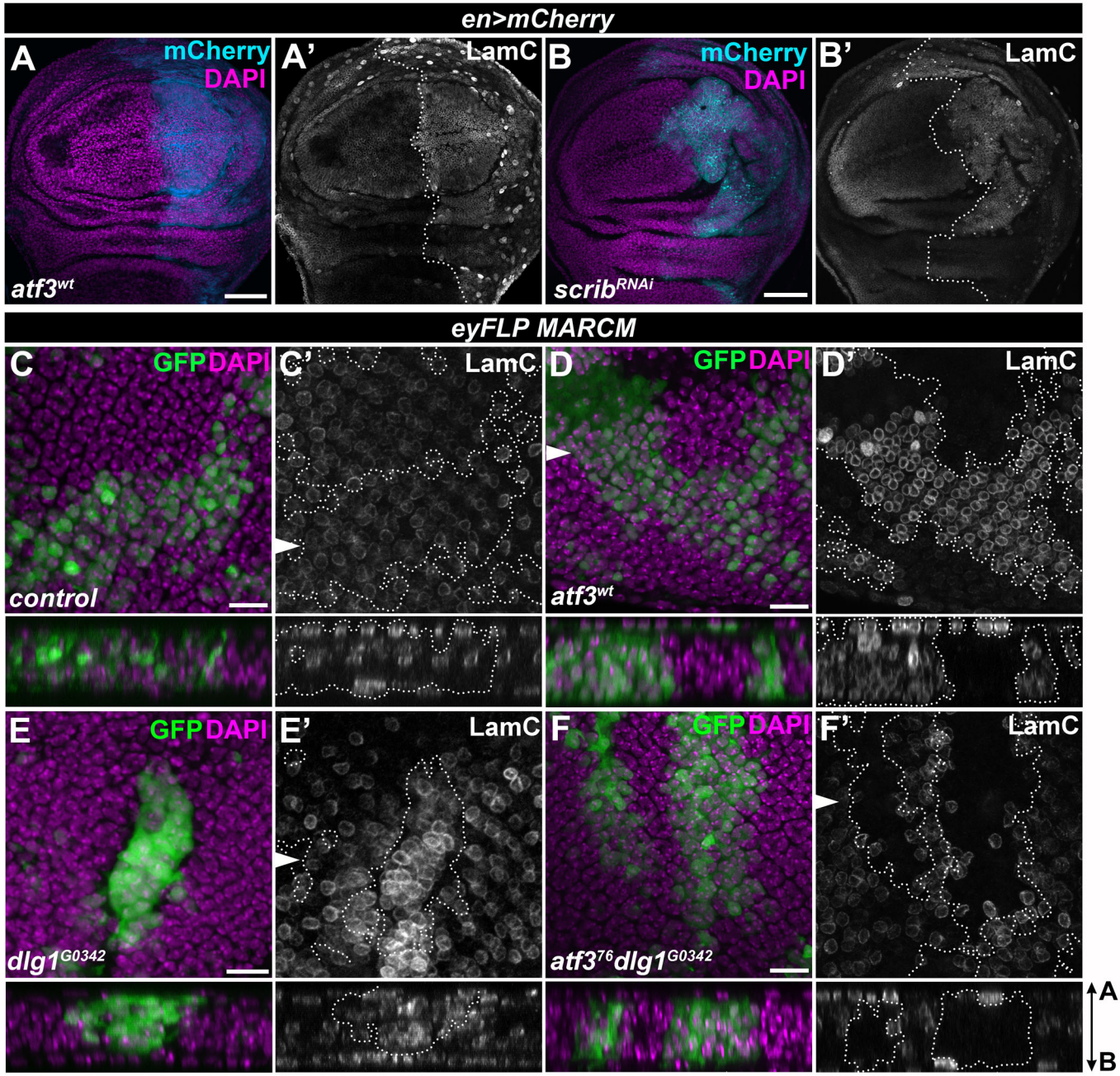
en>mCherry
A
mCherry
DAPI
atf3wt
A'
LamC
B
mCherry
DAPI
scribRNAi
B'
LamC
eyFLP MARCM
C
GFP DAPI
control
C'
LamC
D
GFP DAPI
atf3wt
D'
LamC
E
GFP DAPI
dlg1G0342
E'
LamC
F
GFP DAPI
atf376dlg1G0342
F'
LamC
A
B

Figure 7

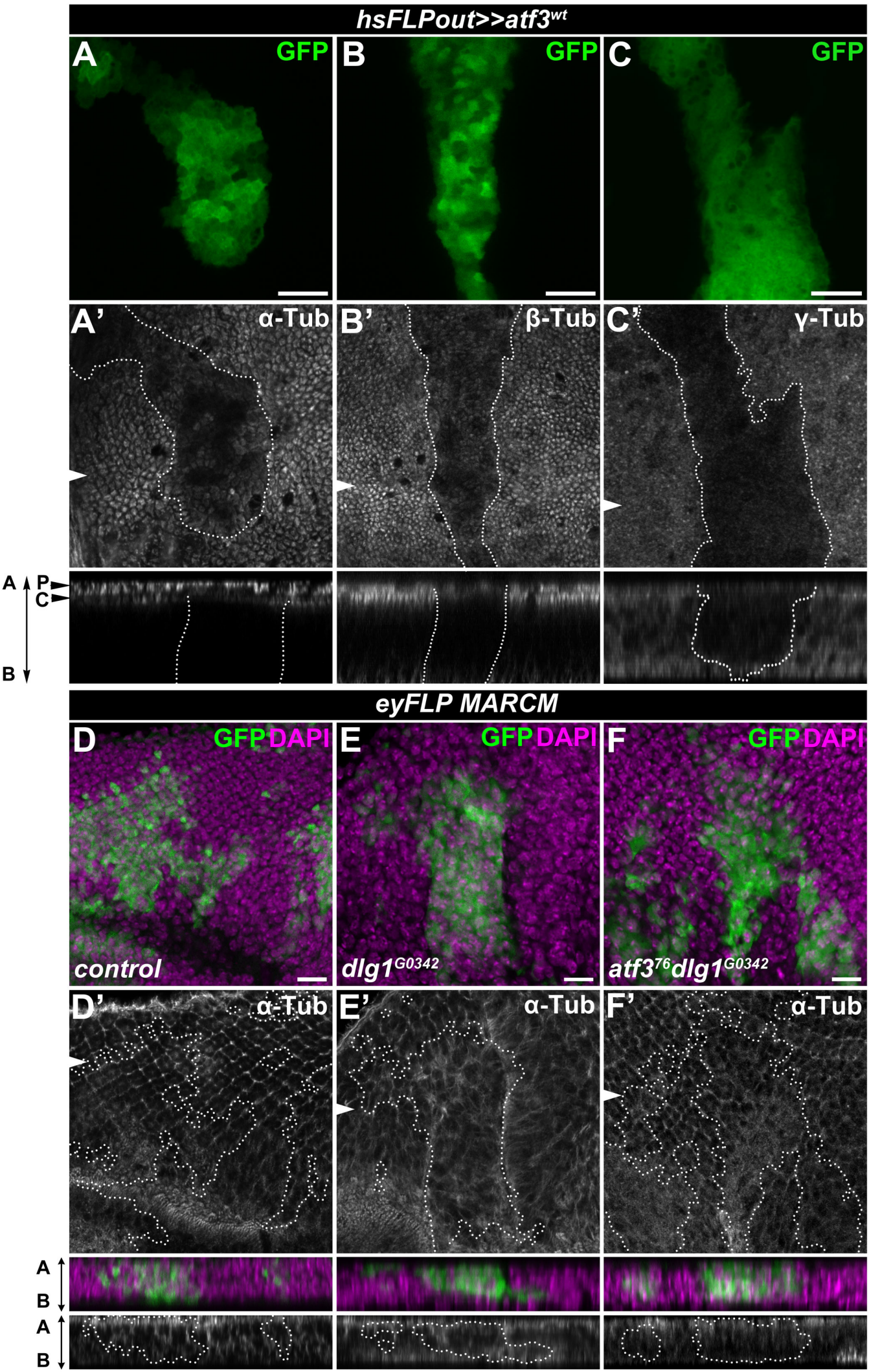
hsFLPout>>atf3wt
A
GFP
B
GFP
C
GFP
A'
α-Tub
B'
β-Tub
C'
γ-Tub
A
P
C
B
eyFLP MARCM
D
GFP DAPI
control
E
GFP DAPI
dlg1G0342
F
GFP DAPI
atf376dlg1G0342
D'
α-Tub
E'
α-Tub
F'
α-Tub
A
B
A
B

Figure 8

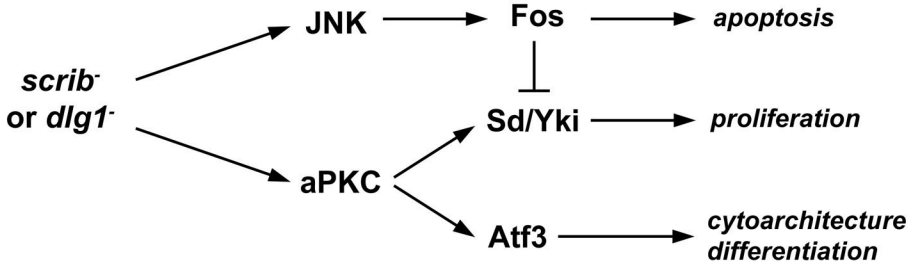
scrib-
or dlg1-
JNK
Fos
apoptosis
Sd/Yki
proliferation
aPKC
Atf3
cytoarchitecture
differentiation

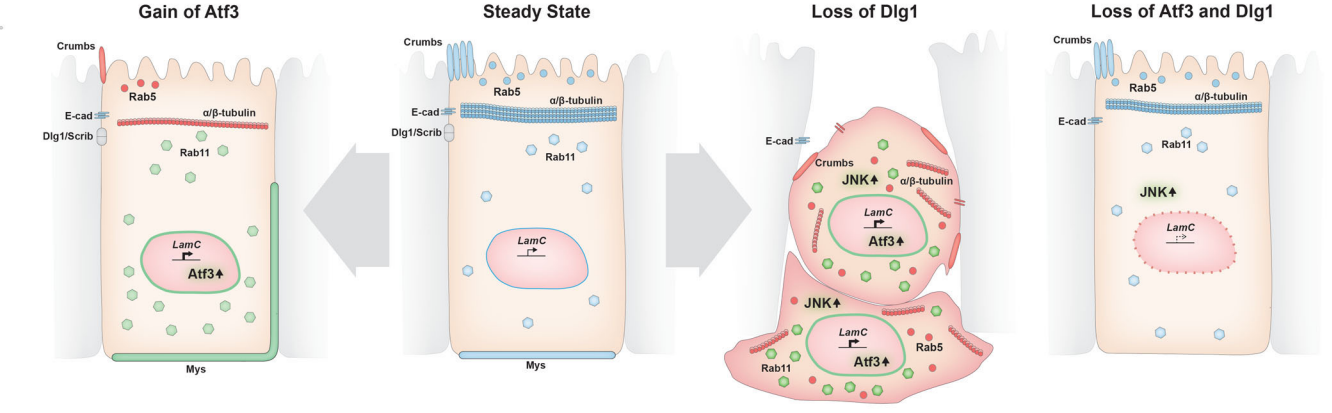
Gain of Atf3
Crumbs
Rab5
E-cad
α/β-tubulin
Dlg1/Scrib
Rab11
LamC
Atf3
Mys
Steady State
Crumbs
Rab5
E-cad
α/β-tubulin
Dlg1/Scrib
Rab11
LamC
Mys
Loss of Dlg1
E-cad
Crumbs
JNK
α/β-tubulin
LamC
Atf3
JNK
LamC
Atf3
Rab5
Rab11
Loss of Atf3 and Dlg1
Crumbs
Rab5
α/β-tubulin
E-cad
Rab11
JNK
LamC